# Arid climate disturbance and the development of salinized lacustrine oil shale in the Middle Jurassic Dameigou Formation, Qaidam Basin, northwestern China

Yuxuan Wang [a], Shang Xu [b], Fang Hao [b], Simon W. Poulton [c], Yuanyin Zhang ,[d] *,Tianxu Guo [d], Yangbo Lu [a] ,Nan Bai [a]

a. Key Laboratory of Tectonics and Petroleum Resources, Ministry of Education, China University of Geosciences, Wuhan 430074, China

b. School of Geosciences, China University of Petroleum, Qingdao 266580, China

c. School of Earth and Environment, University of Leeds, Leeds LS2 9JT, UK

d. Oil and Gas Survey, China Geological Survey, Beisihuan Road No.267, Haidian district, Beijing 100083, China.

Author: Yuxuan Wang

E-mail address: wyx_cug@163.com

Address: Key Laboratory of Tectonics and Petroleum Resources, Ministry of Education, China University of Geosciences, Lumo Road No.388, Wuhan 430074, China

Author: Shang Xu

E-mail address: xushang0222@163.com

Address: School of Geosciences, China University of Petroleum, Changjiangxi Road No.66, Qingdao 266580, China

Author: Fang Hao

E-mail address: haofang@cug.edu.cn
Address: School of Geosciences, China University of Petroleum, Changjiangxi Road No.66, Qingdao 266580, China

Author: Simon W. Poulton
E-mail address: S.Poulton@leeds.ac.uk
Address: School of Earth and Environment, University of Leeds. Woodhouse, Leeds LS2 9JT, UK

*Corresponding author: Yuanyin Zhang
E-mail address: yuanyinshou@163.com
Address: Oil and Gas Survey, China Geological Survey, Beisihuan Road No.267, Haidian district, Beijing 100083, China

Author: Tianxu Guo
E-mail address: 253307350@qq.com
Address: School of Geosciences, China University of Petroleum, Changjiangxi Road No.66, Qingdao 266580, China

Author: Yangbo Lu
E-mail address: luyb@cug.edu.cn
Address: Key Laboratory of Tectonics and Petroleum Resources, Ministry of Education, China University of Geosciences, Lumo Road No.388, Wuhan 430074, China

Author: Nan Bai

E-mail address: 893671588@qq.com

Address: Key Laboratory of Tectonics and Petroleum Resources, Ministry of Education, China University of Geosciences, Lumo Road No.388, Wuhan 430074, China

# Abstract:

The lacustrine Dameigou organic-rich shale of the northern Qaidam Basin is a particularly promising play for recent unconventional oil and gas exploration in China. Deposition was associated with arid intervals during the otherwise humid Middle Jurassic, but the depositional mechanism and organic matter enrichment processes are poorly understood. This study integrates high-resolution organic and inorganic geochemical proxies with detailed sedimentary observations for samples from the Chaiye (CY1) borehole, located in the Yuqia Depression, to investigate the depositional environment and development of the Dameigou shales. Four major lithofacies, including sandy mudstones, oil shale, organic-rich mudstone, and argillaceous mudstone, were identified through detailed microscopic observation and mineralogical analyses. Geochemical paleoclimate proxies (CIA, Fe/Mn and Mg/Ca) indicate that humidity fluctuations primarily drove the lithofacies variation. Other geochemical proxies, including terrigenous supply ($Al_2O_3$, $Ti_2O$ and regular sterane), lake salinity (Sr/Ba, S/TOC and Ga), redox conditions (V/Cr, U/Th and Pr/Ph), and primary productivity ($Ba_{xs}$, $P_{xs}$) indicate that climatic variability exerted a first-order control on the chemical evolution of the lake and the development of organic-rich shale in the Yuqia area. During arid intervals, fresh water supply through precipitation and river

runoff weakened, leading to an increase in salinity and water column stratification. As a result, surface water became brackish and oxygen-rich, promoting growth of algae, but density stratification drove the bottom waters to anoxia, providing favorable conditions for organic matter preservation. Recycling of nutrients such as phosphorus under anoxic conditions further promoted eutrophication and high productivity in the surface water, which ultimately promoted the precipitation of carbonate minerals.


## Keywords:

Organic-rich shale; Paleoclimate; Redox history; Saline lake; Water column stratification


## 1. Introduction

Lacustrine organic-rich shale has long been a significant source rock for conventional petroleum, providing more than 20% of the conventional global oil resource (Bohacs et al., 2000). Many of these deposits, including the Green River Formation in America, the Brown Shale in southeastern Asia, and the Aptian-Albian sequences in Brazil, are also significant sources of unconventional oil and gas (Neumann et al., 2003 Katz and Lin, 2014; Burton et al., 2014 Rodriguez and Philp, 2015; Smith et al., 2015). Continental basins are widespread in China, providing extensive lacustrine shales (Hao et al., 2013; Yang et al., 2019) that account for ~85% of conventional reserves (Katz, 1990; Li et al., 1995; Katz et al., 1998). These lacustrine organic-rich shales have become significant exploration targets for shale oil and gas in China (Li et al., 2014; Ma et al., 2016; Hu et al., 2018; Song et al., 2019).

The formation of lacustrine organic-rich shales is particularly sensitive to paleoclimatic conditions (Anderson and Dean, 1988; Wang et al., 2005; Macquaker et al., 2007; Smith et al., 2008). Climate change affects the hydrological regime and alters the relative significance of precipitation and evaporation (Carroll and Bohacs, 1999; Jiang et al., 2007; Kent-Corson et al., 2010; Chamberlain et a1., 2013). Under different climatic conditions, lake water chemistry, primary productivity and terrigenous input may all evolve, which further controls the nature of sedimentation and organic matter enrichment in lacustrine sediments (Carroll and Bohacs, 2001; Doebbert et al., 2010; Hao et al., 2011).

The Qaidam Basin is an important petroleum basin in northwest China (Fig. 1A). Petroleum exploration started in the mid-1950s, and many oil and gas fields were found in the following 60 years (Li et al., 2014). These petroleum resources mainly occur in the seventh member of the Middle Jurassic Dameigou Formation ($J_2d^7$), which has a high organic matter content and was deposited in a lacustrine setting (Yang et al., 2004; Liu et al., 2008; Li et al., 2016; Qin et al., 2018). The Chaiye 1 (CY1) well, located in the Yuqia Sag at an altitude of about 3050 m, was the first lacustrine shale gas parameter well drilled by the China Geological Survey in 2013 (Fig. 1C). Shale adsorption isotherms show that the $J_2d^7$ has a Langmuir adsorption capacity ranging from 0.55-5.93 $m^3/t$, indicating a significant shale gas exploration potential (Wang et al., 2016;

Guo et al., 2018). The sequence stratigraphic framework of the Middle Jurassic Dameigou Formation in Yuqia Sag is well-established (Li et al., 2014; Shao et al., 2015; Shang et al., 2018; Qian et al., 2018), and organic geochemical analyses have indicated large-scale paleoclimatic change during its deposition (Ritts et al., 1999; Wang et al., 2015; Meng et al., 2018; Hu et al., 2019). However, a detailed understanding of climate variability during deposition, particularly with regard to the changing hydrological conditions, remains unclear. Furthermore, links between climate change and deposition of the organic-rich oil shale are poorly understood.

This study presents high-resolution geochemical analyses, combined with a detailed sedimentological description, of the lacustrine shales in the CY1 well of the $J_2d^7$ Formation in the Yuqia Sag. Our aims are to (1) reconstruct the paleoclimatic evolution of the north Qaidam Basin during the late Middle Jurassic; (2) identify variability in hydrological conditions (including paleosalinity and redox condition) linked to regional climate change; and (3) develop a sedimentary model for organic-rich shale development in the Dameigou Formation.

# 2. Geological setting

The Qaidam Basin is located in the northeastern Qinghai-Tibetan Plateau, NW China (Fig. 1A), which is a Mesozoic and Cenozoic intracontinental basin that developed on Precambrian crystalline basement (Ritts and Biffi, 2001; Wang et al., 2006; Ren et al., 2017). It is bounded by the northeast Qilian Mountains, northwest

Altyn Mountains and the southwest Kunlun Mountains (Fig. 1B). The northern Qaidam Basin, covering an area of about $3.4\times10^4$ $km^2$, is one of the most important areas for petroleum resources in the basin (Shao et al., 2014). The Yuqia Sag is situated in the Middle of the northern Qaidam Basin (Fig. 1C) and has significant energy potential due to abundant coal and coalbed methane resources, as well as shale gas exploration potential (Li et al., 2016; Qin et al., 2018). The studied Chaiye 1 (CY1) well (97° 2′ E, 36° 55′ N) is within the Yuqia Sag (Fig. 1C).

The terminal Paleozoic marked an end to a period of transgression in the northern Qaidam Basin. Due to the Indosinian movement, the northern Qaidam Basin was in a steady stage of uplift, resulting in no sediment deposition at this time (Li et al., 2016; Shang et al., 2018; Fig. 1C). At the beginning of the Jurassic, the crust began to subside, with sedimentation due to the effects of regional extension and stress relaxation (Wang et al., 2006). The depocenters gradually moved to the southwestern and eastern parts of the northern Qaidam Basin. Owing to the large-scale eastward migration of the Tarim plate relative to the Qaidam microplate at the end of the Early Jurassic, the regional extensional environment transformed into a compressive environment, and the southern part of the northern Qaidam Basin began to uplift (Chen et al., 2012). The depocenter at this time moved eastward to the Yuqia Sag (Fig. 1C).

Paleogene-Neogene reservoirs provide the main host for oil and gas in the northern Qaidam Basin, and are mostly derived from Middle Jurassic coal-bearing mudstone sequences of the Dameigou Formation (Li et al., 2014; Wang et al., 2015). The

Dameigou Formation is further divided into seven members based on lithology and depositional environment. The first to third members of the Dameigou Formation ($J_2d^1$~$J_2d^3$) were formed during the Early Jurassic, and comprise oil shale and carbonaceous mudstone in the first member, and organic-lean mudstones and sandstones in the second and third members (Fig. 2). The fourth to seventh members of the Dameigou Formation ($J_2d^4$~$J_2d^7$) were formed during the Middle Jurassic. The $J_2d^4$ member is dominated by organic-lean coarse to fine-grained sandstones that deposited in braided river deltas. The $J_2d^5$ member is dominated by carbonaceous mudstones and coal seams that deposited in a meandering river delta with significant terrestrial higher plant input. The $J_2d^6$ member comprises mudstones and interbedded sandstones that deposited in a shallow lake and meandering river delta. The $J_2d^7$ member, which was formed in a lacustrine setting, is composed of sandstones at the bottom, coal seams and carbonaceous mudstones in the middle, and oil shale at the top. This study focuses on the middle and upper part of the $J_2d^7$ member (Fig. 2). We note that some studies (Shao et al., 2014, Meng et al., 2018) define the $J_2d^6$ and $J_2d^7$ members as the Shimengou Formation in the Yuqia area, but here we use the Dameigou Formation terminology to represent the seven members.

# 3. Methods

Core samples (83 in total) from the $J_2d^7$ member were obtained from the CY1 well (Fig. 3), with a core depth ranging from 1900 to 2038 m. Samples were freshly cut after removing weathered surfaces, crushed and powdered to $<74$ μm in an agate mortar.

## 3.1 TOC and Rock-Eval pyrolysis

Samples were subjected to total organic carbon (TOC) content determination and Rock-Eval pyrolysis. TOC content was determined, after pre-treatment with 10% HCl at 60ºC, using a LECO CS 400 carbon-sulfur analyzer at Beijing Research Institute of Uranium Geology (BRIUG), Beijing, China. The analying process followed the Chinese Oil and Gas Industry Standard (G/T) 19145-2003 and the analytical precision was <0.5%. The same sample split was subjected to Rock-Eval pyrolysis using a Rock-Eval II instrument. S1 represents hydrocarbon concentration released after heating to 300ºC. S2 represents the hydrocarbon concentration generated in samples heated from 300-600ºC. The hydrogen index (HI) was calculated according to 100×S2/TOC (Behar et al., 2001).

## 3.2 X-ray diffraction

The whole rock and clay mineral compositon of 77 samples was determined on a Panalytical X'PertPRO MPD X-ray diffractometer (XRD) at the Beijing Research Institute of Uranium Geology (BRIUG), Beijing, China. These shale samples were analyzed at 40 kV and 40 mA with Cu Kα radiation, measured at a scanning rate of 2°/min, with the testing angle ranging from 5° to 90°. The relative mineral percentages were calculated using the area under the curve for the major peaks of each mineral, with correction for Lorentz polarisation (Chalmers and Bustin, 2008).

## 3.3 Major and trace elements

Samples were measured for major and trace element concentrations at the State Key Laboratory of Biogeology and Environmental Geology at the China University of Geosciences (Wuhan). Major elements were analyzed via a Philips PW2404 X-ray fluorescence spectrometer, using fused glass discs consisting of a mixture of the powdered sample heated to a temperature of 1000℃ with flux ($Li_2B_4O_7$) at a proportion of 1:8, with a weight of 5.0 g. Precision and accuracy were better than 5% for all major elements (reported as oxides).

Trace element concentrations were determined on a PerkinElmer Elan DCR-e standard inductively coupled plasma-mass spectrometer (ICP-MS). The samples were placed in an oven and dried at 105°C for 12 h. Samples were then accurately weighed (50 ± 1 mg) and placed in a Teflon crucible. 1.5 mL of high purity nitric acid ($HNO_3$) and 1.5 mL of high purity hydrofluoric acid (HF) were then added to the sample, and the closed crucibles were heated for 48 h at 190° C. After cooling, the samples were heated to dryness and then 1 mL $HNO_3$ was added and evaporated to dryness. Finally, 3ml 30% $HNO_3$ was added, and the sealed samples were heated for 48 h at 190°C. Analytical precision for trace element concentrations was better than ±5%.

# 4. Results

## 4.1 Lithofacies description

Four major lithofacies of the Dameigou Formation ($J_2d^7$) mudstone in CY1 are shown in Figs. 3 and 4, including the sandy mudstones, oil shale, organic-rich mudstone, and argillaceous mudstone. An obvious variation in lithofacies assemblages is observed (Fig. 3), with sandy mudstone mainly occurring at the top and bottom of the study section, and this comprises different types of bedding and bioturbation (Fig. 3). The sandy mudstone is mainly composed of coarse-grained detrital minerals, including euhedral quartz and feldspar (Fig. 4A).

The thick-bedded organic-rich mudstone, occurring in the middle and lower section, is the major type of shale lithofacies (Fig 3). Horizontal and small-scale cross bedding is apparent. Under the microscope, this mudstone is characterized by high organic matter content with abundant fine-grained feldspar, quartz and clay minerals (Fig 4.B). The oil shale bed, which is ~8 m thick (Fig 3), occurs in the upper part of the section. This unit has a notable growth of carbonate minerals, such as calcite and dolomite. However, the detrital mineral contents, including quartz, feldspar and clay minerals is relatively lower (Fig. 4C, D). Horizontal laminae are prevalent in the oil shale, comprising fine-grained clastic layers such as organic-rich mudstones and cryptocrystalline carbonate layers (Fig. 3). The cryptocrystalline carbonate layers have distinct boundaries which are partly wavy at the micro-scale (Fig. 4D). Microscopic fossils, including algal aggregates and plankton residue are also frequently observed, and are preserved parallel to the bedding or stacked as lenticles (Fig. 4E, F, G). The argillaceous mudstones are relatively concentrated in the upper part of the study section. This facies is organic lean and mainly composed of clay minerals, with a small percentage of quartz and feldspar (Fig. 4H).

## 4.2 Mineralogical characteristics

The XRD results are plotted in Figure 5 and tabulated in Table 1. The sandy mudstone is characterized by a high proportion of silicate minerals (quartz + K-feldspar + plagioclase), ranging from 20.9 to 75.8 wt.%, with an average of 36.2 wt.%; low carbonate content (calcite + dolomite + aragonite + siderite), ranging from 0 to 31.6 wt.%, with an average of 6.0 wt.%; and a high amount of clay minerals, ranging from 38.0 to 74.8 wt.%, with an average of 57.8 wt.% (Fig. 5; Table 1). Quartz is the dominant mineral in the silicates, ranging from 17.2 to 50.3 wt.% (avg. 32.7 wt.%). K-feldspar and plagioclase comprise less than 3.0 wt.% (avg. 2.3 wt.% and 1.2 wt.%, respectively). The average proportion of calcite and siderite is 1.1 wt.% and 4.9 wt.%, respectively. Dolomite is rarely found in this sequence.

In the organic-rich mudstone, the amount of silicate minerals decreases to 30.6 wt.% on average, with a range from 16.1 to 77.6 wt.%; the amount of carbonate increases to 8.1 wt.% on average, with a range of 0 to 47.3 wt.%; and the average amount of clay minerals slightly increases to 61.3 wt.%, with a range of 14.7 to 76.6 wt.%. Compared to the sandy-mudstone, the average amount of feldspar in the organic-rich mudstone shows no apparent change. The average content of K-feldspar slightly decreases to 1.6 wt.%, while plagioclase slightly increases to 2.5 wt.%. The quartz content also decreases, and ranges from 11.1 to 77.3 wt.%, with an average of 26.4 wt.%. Calcite and dolomite are very minor in this lithofacies. The siderite ranges from 0 to 47.3 wt.% (avg. 7.8 wt.%).

For the oil shale, the silicate fraction drops to 26.5 wt.% on average, with a range of 8.8 to 30.2 wt.%; the clay mineral fraction decreases to 38.5 wt.% on average, with a range of 10.0 to 47.8 wt.%; the amount of carbonate increases up to 35.0 wt.% on average (Fig. 5; Table 1). Carbonate minerals, including calcite, dolomite and aragonite, with average contents of 12.6 wt.%, 3.1 wt.% and 17.8 wt.%, respectively, dominate in the oil shale. The mineral composition of the argillaceous mudstone is similar to the organic-rich mudstone, with a medium silicate content (avg. 31.3 wt.%) and low carbonate content (avg. 9.2 wt.%). Clay becomes a dominant mineral fraction, ranging from 22.1 wt.% to 74.5 wt.%, with an average of 59.5 wt.%.

## 4.3 Organic matter characteristics

The results of TOC analyses and Rock-Eval pyrolysis are plotted in Fig. 6 and Fig. 7. We divide the study section into three units based on TOC content, including two low-TOC units (unit 1 and unit 3), and a high-TOC unit (unit 2). The sandy mudstone has the lowest TOC content, between 0.3 and 2.9 wt.% (avg. 0.8 wt.%). It also has

S1+S2 and HI indices between 0.2 and 6.3 mg/g (avg.1.23 mg/g), and 82 and 471 mg/g (avg. 191 mg/g), respectively, suggesting low organic matter abundance and primarily gas generation potential. The organic-rich mudstones are characterized by TOC contents between 0.65 and 6.5 wt.% (avg. 3.6 wt.%), S1+S2 between 1.0 and 13.9 mg/g (avg. 7.4 mg/g), and HI between 146 and 508 mg/g (avg. 240 mg/g), indicating high organic matter richness and good gas generation potential.

Oil shale samples collected from the upper part of unit 2 have the highest organic matter contents and HI values. The TOC contents range between 3.9 and 6.7 wt.% (avg. 4.3 wt.%), and S1+S2 values are between 14.8 and 22.9 mg/g (avg. 18.4 mg/g). The HI is between 398 and 426 mg/g (avg. 413 mg/g), indicating type II and II/III organic matter, with partial oil generation potential. Most of the argillaceous mudstones of unit 3 have low organic matter abundance and HI values. The TOC contents range from 0.3 to 5.0 wt.% (avg. 1.6 wt.%) and S1+S2 ranges from 0.02 to 10.6 mg/g (avg. 3.39 mg/g). From the bottom of unit 1 to the top of unit 3, the TOC content, hydrocarbon generation potential (S1+S2), and hydrogen index (HI) of shale samples show a similar trend (Fig. 6A, B, C). The trends in TOC vary within different units, with no obvious change in TOC in unit 1. However, an upwards increase is evident in unit 2, climbing from ~3 to ~6 wt.%. In unit 3, the TOC content rapidly drops to ~0.5 wt.%. Both S1+S2 and HI follow a similar pattern.

## 4.4 Major element geochemistry

Geochemical parameters are shown in Table 2. Major element analyses show that CaO dominates in the oil shale samples, ranging from 17.6 wt.% to 47.9 wt.% (avg. 29.3 wt.%). However, CaO is less than 1 wt.% in the other three lithofacies (sandy mudstone, organic-rich mudstone, argillaceous mudstone). $SiO_2$, $Al_2O_3$ and $Fe_2O_3$ are major constituents in most of the samples, with average concentrations of 49.1, 20.1, and 7.3 wt.%, respectively. The average concentrations of $K_2O$ and MgO are 2.3 and 1.8 wt.%, respectively. Other elements, including MnO, $Na_2O$, $TiO_2$ and $P_2O_5$, have average concentrations below 1 wt.%. Fe/Mn and Mg/Ca ratios remain relatively high in unit 1 (Fig. 6D, E). Then, the Fe/Mn ratios decrease modestly in unit 2 and reclimb in unit 3 (Fig. 6D), whereas Mg/Ca ratios remain high in the organic-rich shale, then drop in the oil shale in unit 2 and remain low in unit 3 (Fig. 6E). The terrigeneous indicators, $Al_2O_3$ and $Ti_2O$, show similar variability, and remain relatively high through most of the study section, with the exception of some very low contents, for example in the oil shale (Fig. 6F, G).

Regional weathering conditions and paleoclimate may be evaluated by the chemical index of alteration (CIA) weathering proxy (Nesbitt et al., 1982; Young and Nesbitt, 1999; Cullers and Podkovyrov, 2002), which is calculated by CIA = $Al_2O_3/(Al_2O_3+CaO^*+Na_2O+K_2O) \times 100$ (where CaO* represents CaO incorporated into silicate minerals). Therefore, it is necessary to subtract the CaO incorporated into carbonates (calcite, dolomite) and phosphates (assuming all the $P_2O_5$ is present as apatite) (Fedo et al., 1995). As Ca is preferentially removed relative to Na during chemical weathering (Mclennan, 1993), the remaining number of moles is adopted if it is less than that of $Na_2O$; otherwise, CaO* is assumed to be equivalent to $Na_2O$. The CIA indicator shows low values in the middle of unit 1 and persistently high values in the bottom to middle of unit 2 (Fig. 6H). Then CIA values show a slight upwards decrease in the remaining organic-rich shale, followed by a marked decrease in the oil shale. In unit 3, the CIA indicator rises rapidly to higher values.

## 4.5 Trace element geochemistry

We use a variety of geochemical indicators to reconstruct paleoenvironmental change in the basin (Fig 7; Table 2). Sr/Ba ratios exhibit an extremely high peak in oil shale samples, whereas very low ratios occur in other lithofacies (Fig. 7D). Ga contents show similar trends (Fig. 7E), with high and relatively stable contents in unit 3, a slight decline in organic-rich shale samples, a significant drop in the oil shale samples of unit 2, and a rapid increase in unit 3.

Elemental enrichment factors (EF) were calculated as: $X_{EF}=(X/Al)_{sample}/(X/Al)_{PAAS}$. The $V_{EF}$, $Cr_{EF}$ and $U_{EF}$ ratios demonstrate the same pattern, with low values in units 1 and 3, but much higher values in unit 2, particularly in oil shale samples (Fig. 7 F, G, H). The concentrations of Ba and Si in "excess" of normal terrigenous content ($Ba_{xs}$, $P_{xs}$) are considered to represent the biogenic fraction for these elements, and are calculated by $X_{xs} = X_{total}-(Al \times [X/Al]_{PAAS})$, where X is the concentration of the element of interest, and PAAS represents post-Archean average shale (PAAS). Both $Ba_{xs}$ and $P_{xs}$ contents are very high in the oil shale samples. However, in other samples, $Ba_{xs}$ and $P_{xs}$ are close to zero, although there are some isolated peaks in the middle part of unit 2.

# 5. Discussion

## 5.1 Paleoclimatic reconstruction

Generally, CIA values of between 50 to 65 repesent an arid climate with low chemical weathering intensity, values of 65-85 indicate a temperate climate with a moderate chemical weathering rate, and values > 85 reflect a hot and humid climate with strong chemical weathering intensity (Nesbitt and Young, 1982). The CIA values are generally high (Fig. 6H), with stable high values in the upper part of unit 1 and the lower part of unit 2, suggesting a long-term interval of intense chemical weathering rate. However, CIA values exhibit a slow decline through the uppermost organic-rich shale, with low values in the oil shale at the top of unit 2, as well as in the middle of unit 1 (Fig. 6H). This shows that the paleoclimatic regime was periodically altered, with transitions to more arid conditions.

Fe/Mn and Mg/Ca ratios may also be used as proxies to characterize paleoclimatic conditions (Reheis, 1990), although Fe/Mn ratios may also be affected by water column redox conditions. Manganese tends to remain high in sediments deposited under arid conditions, but may be lower under relatively humid conditions. By contrast, with more intense chemical weathering under humid conditions, Fe is retained in the weathered sediment (e.g., Poulton and Raiswell, 2002). Therefore, high Fe/Mn ratios tend to represent hot-humid environments, whereas low ratios commonly occur in a cold-dry climate (Reheis, 1990). In terms of Mg/Ca, high ratios in alkaline lakes may indicate a warm-humid climate (Lermen et al., 1995). Thus, high Fe/Mn and Mg/Ca ratios support the suggestion, based on the CIA proxy, of a dominantly warm and humid climate during deposition of the 7th member of the Dameigou Formation. However, low values for both Fe/Mn and Mg/Ca support short-term and high-intensity arid climate disturbance during deposition of the oil shale section in the upper part of unit 2 (Fig. 6D, E).

## 5.2 Terrigenous supply

### 5.2.1 Clastic input

The intensity and rate of clastic influx directly affects the mineral composition and organic matter characteristics of lacustrine black shale (Johnson Ibach, 1982; Rimmer, 2004). A moderate rate of deposition is beneficial for the burial efficiency of organic matter, but fast depositional rates dilute the organic matter (Canfield, 1994; Wang et al., 2019). The aluminum (Al) and titanium (Ti) content of sediments may be used to evaluate the relative clastic influx rate (Rimmer, 2004; Wang et al., 2020). Aluminium is principally present in clays, feldspars and other aluminum silicate minerals, while titanium is usually related to clays and heavy minerals (e.g., ilmenite and rutile).

In the study section, Al and Ti show a similar pattern: persistent high values through the humid climate zones, with two short-term transitions to lower values in the arid climate zones (Fig. 6F, G). This indicates that the nature of the clastic sediment influx was controlled by paleoclimate. Unit 1 was fluvially-influenced, comprising lacustrine-swamp and meandering fluvial facies (Fig. 3), and under the humid climatic conditions, chemical weathering was intense. Clastic sediment was transported into the sedimentary basin, forming the sandy mudstone and minor intervals of organic-rich mudstone. However, when the climate became more arid, the size of the sedimentary basin diminished, resulting in deposition of coarse-grained siltstone-sandstone, and even conglomeratic sandstone in the middle of unit 1.

Units 2 and 3 developed in a lake delta and deep lake sedimentary system. Under humid climatic conditions, high intensity runoff maintained the deep-water lacustrine environment. The detrital material delivered to the basin by rivers mainly comprised fine-grained minerals, such as feldspar and quartz. During arid intervals, due to the simultaneous reduction of weathering and fluvial intensity, less detrital material deposited in the deep-water lakes. Therefore, authigenic minerals such as calcite, dolomite and aragonite dominated during deposition of the oil shale intervals.

### 5.2.2 Organic matter sources

The nature of the paleoenvironment controls the source of organic matter in lacustrine sediments, and different types of organic matter directly determine the quality of the source rocks (Tissot and Welte, 1984; Hedges et al., 1994; Zakir Hossain et al., 2009). The source of lacustrine organic matter may be divided into intrabasinal organic matter and extrabasinal organic matter, of which the intrabasinal organic matter represents productivity via aquatic organisms in the lake itself, whereas extrabasinal organic matter is mainly derived from terrestrial sources transported by rivers and wind. The organic matter classification is defined by a cross-plot of HI vs. $T_{max}$ (Qin et al., 2018), and the data fall into four groups based on lithology (Fig. 8A). Sandy mudstones and organic-rich mudstones (including coal beds) mainly comprise types III or type $II_2$ kerogen, representing a dominant source from higher terrestrial plants. However, the kerogen type changes to type $II_1$ for most organic-rich shale samples, and type I for oil shale samples, which documents a primary source from within the basin.

The organic matter composition provides further information on the source of organic matter. Different organic substances have different $C_{27}$, $C_{28}$, and $C_{29}$ sterol contents (Peters et al., 2005), however, lower aquatic organisms are abundant in $C_{27}$ sterols and higher plants tend to be rich in $C_{29}$ sterols (Ghassal et al., 2018; Waples and Machihara, 1990). From the sandy mudstone in unit 1 to the oil shale in unit 2, the type of organic matter evolves: the significance of higher plants decreases while plankton progressively increases through the section (Fig. 8B). During the humid climate period, surface runoff strengthened, and larger organic matter particles such as higher plants, were readily transported to lakes (or swamps) to deposit. By contrast, under arid condtions, transportation via rivers was greatly weakened, thus decreasing the organic matter input from higher plants, leading to an increased contribution from lower plankton or algae.

## 5.3 Water column chemistry

### 5.3.1 Paleosalinity

Trace element proxies such as strontium/barium (Sr/Ba) and gallium (Ga) concentration may be used to infer paleo-salinity in lacustrine basins (Pais and Jones, 1997; Wei and Algeo, 2019). The chemical properties of Sr and Ba are similar, but they respond differently to increasing salinity (Lan et al., 1987; Zheng and Liu, 1999). In terrestrial sediments, strontium is liberated more quickly than barium during weathering, causing low Sr/Ba ratios (~1.4) in freshwaters (Yang et al., 2004a; Yang et al., 2004b). By contrast, there are much higher Sr/Ba ratios (~39) in seawater because of their different concentrations (Sr is 8.1 mg/l and Ba is 0.021 mg/l) (Krauskopf, 1956). These fundamental differences make the Sr/Ba ratio a proxy for the salinity of an ancient water body (Deng and Qian, 1993; Zheng and Liu, 1999; Wei et al., 2018; Wei and Algeo, 2019). Generally, Sr/Ba ratios of <0.2, 0.2-0.5, and >0.5 are thresholds for sediments deposited under freshwater, brackish and seawater conditions (Wei and Algeo, 2019). Gallium is primarily derived from quartzose and feldspathic silicate rocks and is often adsorbed onto clay minerals (Couch, 1971; Chen et al., 1997). This process leads to higher Ga contents in freshwater sediments relative to marine sediments (Bowen, 1982; Salminen et al., 2005).

The Sr/Ba ratios are extremely high (avg. 1.35) in oil shale samples and adjacent organic-rich shale samples, but are very low in other samples (avg. 0.19) (Fig. 7D). This indicates that during organic-rich shale deposition, the lake maintained a relatively stable freshwater environment. By contrast, in the oil shale section, the salinity of the lake increased sharply and then quickly desalinated and returned to the previous level. Gallium concentrations show the same trend as Sr/Ba ratios and thus support this inference (Fig. 7E). Thus, this lacustrine setting began to salinize in the middle part of the organic-rich shale in unit 2, and then in the oil shale section, both the rate and intensity of lake salinization increased sharply.

The ratio S/TOC is an additional, frequently used paleosalinity indicator (Berner and Raiswell, 1984; Wei and Algeo, 2019). When the TOC content of samples is > 1 wt.%, the S/TOC thresholds are > 0.5 for seawater conditions, and < 0.5 for freshwater conditions (Wei et al., 2018). In the study section, samples from the oil shale in unit 2 and the organic-rich shale in unit 1 have high S/TOC ratios, which supports salinization during deposition of these lithologies (Fig. 7C). These combined results for Sr/Ba, Ga and S/TOC suggest that salinity was mainly controlled by climate, since there is no obvious evidence of transgression in the study area. Thus, under a humid climate, the lake had sufficient water supply to maintain freshwater conditions, whereas during deposition of the oil shale, the rapid development of arid conditions resulted in salinization.

### 5.3.2 Redox conditions

Redox conditions in the water column can be evaluated by the degree of enrichment of redox-sensitive elements such as V, Cr and U (Calvert and Pedersen, 1993; Dean et al., 1997; Tribovillard et al., 2006; Wang et al., 2019; Algeo and Li, 2020; Algeo and Liu, 2020). Both V and Cr are soluble under oxic conditions, but may be enriched under reducing conditions (Morford and Emerson, 1999). However, the removal of V occurs coincident with the beginning of denitrification, whereas the removal of Cr occurs later as conditions become more reducing towards the end of denitrification (Pattan et al., 2005). These behaviours are widely used to evaluate paleoredox conditions in the column (Tribovillard et al., 2006).

Uranium exists in the form of $UO_2(CO_3)_3^{4-}$ in oxic seawater, where it is highly solubile. However, in reducing environments, soluble U(VI) is reduced to U(IV) coincident with the reduction of Fe(III) to Fe(II), causing U enrichment in the sediments (Chaillou et al., 2002; McManus et al., 2005). This removal process of U from the water column to the sediments is considered to be accelerated by organometallic ligands in humic acids (Zheng et al., 2002a,b; McManus et al., 2005). Hence, U abundance in sediments is commonly used to indicate redox conditions and organic matter preservation (Algeo and Maynard, 2004). Based on these systematics, all of the redox proxies we employ ($V_{EF}$, $Cr_{EF}$ and $U_{EF}$) suggest oxic conditions throughout deposition of most of the 7$^{th}$ member of the Dameigou Formation (Fig. 7F, G, H). However, during deposition of the oil shale, the water column was dominantly anoxic (Fig. 7).

Reactive organic matter produced in the photic zone is more enriched in hydrogen than vascular land plant and thus more sensitive to redox conditions (Tissot and Welte, 1984). The HI can therefore also serve as an indicator of redox conditions. The HI is higher in the oil shale (avg. 305 mg/g TOC) relative to the organic-rich mudstone, argillaceous mudstone and sandy mudstone (avg. 257, 185 and 129 mg/g TOC, respectively), indicating more reducing bottom water conditions during deposition of the oil shale (Fig. 6). The pristane/phytane (Pr/Ph) ratio is also widely used as an index to interpret redox conditions (Didyk et al., 1978; Hughes et al., 1995). Based on the analyses of about 100 crude oil samples from major petroliferous basins in China, Mei and Liu (1980) suggest that Pr/Ph ratios <0.8 indicate anoxic environments, Pr/Ph ratios between 0.8 and 2.8 indicate suboxic conditions, and Pr/Ph ratios >2.8 indicate dysoxic to oxic settings. The organic-rich mudstone and argillaceous mudstone have Pr/Ph ratios between 2.0 to 2.2, suggesting suboxic bottom water conditions. By contrast, Pr/Ph ratios are much lower in the oil shale at 0.8, supporting anoxic bottom water conditions (Fig. 8D). A plot of $Pr/nC_{17}$ versus $Pr/nC_{18}$ also indicates that the oil shale deposited in a more reducing environment relative to the other lithofacies (Fig. 8C).

Combining the evidence from organic and inorganic geochemical data thus strongly suggests that the lake was anoxic at times of arid climate, and oxic under humid climatic conditions. This may also partly relate to the tectonic regime, whereby the Yuka Sag coincided with a tectonic subsidence stage during the middle Jurassic dry climate period (Shao et al., 2014; Li et al., 2014). Hence, because the rate of tectonic subsidence was higher than the rate of lake-level decline due to climate drying, the system remained relatively deep-water for a considerable time, allowing deposition of the oil shale sections.

## 5.4 Paleoproductivity

Excess Phosphorus ($P_{xs}$) and Barium ($Ba_{xs}$) are commonly used as proxies to evaluate relative levels of productivity (Nameroff et al., 2002; Piper and Perkins, 2004; Algeo and Rowe, 2012; Schoepfer et al., 2015; Wang et al., 2020). In the study section, both $Ba_{xs}$ and $P_{xs}$ are high in the oil shale and adjacent organic-rich shale samples, but are low throughout the rest of the succession (Fig.7 H, I), suggesting elevated primary productivity during oil shale sedimentation. Evidence from organic geochemistry also supports this inference. The plots of Pr/nC17 versus Pr/nC18 plot, and GI versus Pr/Ph, suggest that the organic matter in the oil shale was deposited under enhanced salinity (Fig. 8C), and derives from algae and microorganisms. This is further supported by large quantities of algal material in the oil shale samples, suggesting algal blooms at this time.

These observations suggest that, during deposition of the oil shale, the arid climate led to a decrease in the size of the lake, with strong salinization of the water. This saline environment was suitable for the survival of algae and halophilic bacteria, leading to an intense algal bloom during this period. Dissolved oxygen in the lake water was rapidly consumed by microbial respiration, and the deeper lake waters became anoxic.

At the same time, algal growth in surface waters may have decreased gas exchange between water and air, further promoting anoxia.

Recycling of major nutrients (particularly P) under anoxic conditions would also have exerted a positive feedback on productivity (Benitez-Nelson, 2000; Sageman et al., 2003). In particular, P is preferentially released from organic matter during microbial remineralization, while reductive dissolution of iron (oxyhydr)oxide minerals also releases adsorbed phosphate to solution (e.g., Krom and Berner, 1981; Froelich et al., 1988; Slomp et al., 1996a,b; Anschutz et al., 1998; Xiong et al., 2019). Some of the released P may be fixed in the sediment, via sink-switching to other phases such as carbonate fluorapatite or vivianite (e.g., Van Cappellen and Ingall, 1994; Slomp et al., 1996a,b; Xiong et al., 2019), but under anoxic water column conditions, a significant proportion of the P may be recycled back to the water column, thus potentially stimulating further productivity (Ingall and Jahnke, 1994, 1997; Slomp et al., 2002, 2004). This is exemplified by Lake Kivu, which is a salinity stratified lake in East Africa. The lake has a phosphorus concentration of ~70 mg/L in bottom waters, which results in substantial algal blooms and an organic carbon content in the lake sediments of up to ~15 wt.% (Anadon et al., 1991). For ancient lakes, salinized lacustrine oil shale with typical carbonate lamina also occurs in the Shahejie Formation of the Bohai Basin, East China, which has been suggested to have been influenced by this recycling of phosphorus (Wang and Zhong, 2004, Zhu et al., 2004).

## 5.5 Mechanisms of lacustrine oil shale development under arid climatic conditions

Previous studies have shown that lacustrine shale deposition is controlled by multiple factors, including climate, salinity and water depth (Anderson and Dean, 1988; Dean et al., 1999; Wang and Zhong, 2004). The oil shale of the 7th member of the Dameigou Formation in the Qaidam Basin exhibits typical carbonate lamina structure, which deposited under high-productivity, high-salinity, reducing conditions. Various studies have shown that deposition of laminated oil shale is closely related to the stratification of the lake water (Dean et al., 1999; Zhu et al., 2005; Wang et al., 2012). Due to the development of arid climatic conditions (Hu et al., 2017), freshwater supply to the Yuqia Lake Basin rapidly decreased, leading to the gradual salinization of the original freshwater lake. Due to the difference in density, the lake water formed a stable saline-stratified environment, with oxic, lower salinity surface waters (Fig. 9A). These conditions were conducive to algal organisms, generating very high rates of primary productivity in surface waters.

The salinity of mid-depth water likely varied in relation to the local paleoclimate, with consequent shifts in the depth of the halocline (Jin and zhu, 2006; Liu et al., 2015). Although most plankton stuggle to survive under saline conditions, halophilic bacteria may breed in large numbers in this layer (Kemp, 1996). Bottom waters were highly saline, and dissolved oxygen was rapidly consumed, producing an anoxic environment. The lake stratification was stagnant, ensuring a long-period of anoxic and saline conditions in the bottom water, thus providing good preservation potential for organic matter. Furthermore, due to the lack of oxygen in the bottom water, nutrients such as phosphorus were effectively recycled back to the water column, enhancing eutrophication. Thus, both elevated primary productivity and the enhanced preservation potential were crucial for the enrichment of organic matter in the oil shale.

In saline lacustrine environments, deposition of carbonate minerals is usually controlled by $CO_2$ in the lake water (Lallier et al., 1996; Scholle et al., 1983). This depends on a dynamic equilibrium between $CO_2$ consumption by plants and microorganisms during photosynthesis, and $CO_2$ release by respiration and organic matter degradation. During periods of algal blooming, dissolved $CO_2$ in the lake water would be rapidly consumed. Indeed, Scholle et al. (1983) found that in highly eutrophic lakes, the rate of $CO_2$ consumption can reach 1g/m$^2$d, causing the pH of lake water to rise above 9.0. Under dry climatic conditions, there was little surface runoff and precipitation, which maintained stratification, and at the same time, input of terrigenous minerals and organic matter was maintained at a low level. Enhanced photosynthesis consumed $CO_2$ in the upper water of the lake, causing $CaCO_3$ to become oversaturated, thereby precipitating carbonate minerals as laminae within the oil shale (Fig 3D).

However, under humid conditions, freshwater was continuously introduced by precipitation and surface runoff, and the lake water was well mixed (Fig 9B). At this time, productitivy in the water column was at a normal level, resulting in only moderate formation and preservation of organic matter. At the same time, more organic matter and detrital minerals were imported from land sources. The input of terrigenous material, including detrital quartz, feldspar and organic matter from higher plants increased significantly, forming the organic-rich shale horizons in the 7$^{th}$ member of the Dameigou Formation.

# 6. Conclusions

Our combined study of the geochemistry and sedimentology of the 7$^{th}$ member of the late Middle Jurassic Dameigou Formation of northern Qaidam, provides new insight into the mechanisms responsible for the deposition of organic-rich sediments in this setting. The environment was prone to climate change, with humid periods interspersed with intervals of high-intensity arid conditions. This paleoclimatic evolution had a strong influence on the depositional setting, which controlled the development of organic-rich shales in this lacustrine setting. Climate change altered surface runoff, which gave rise to the deposition of different shale lithofacies. In particular, the changing climate regime influenced the salinity and redox evolution of the lake water. During humid periods, the water column was well-mixed with significant freshwater supply.

Under arid conditions, however, insufficient freshwater supply led to lake salinization and stratification. Vertical water circulation was inhibited, causing the development of anoxic and saline conditions in the bottom water. This ultimately led to eutrophication of the lake water, enhancing rates of primary productivity. The remineralization of sinking organic matter consumed dissolved oxygen in the surface lake water, and oxygen levels may also have been hindered by limited gas exchange between the water and the air. The subsequent development of persistent anoxia induced the recycling of nutrients such as P, which further promoted and maintained high productivity in the lake.

These processes were responsible for oil shale development and organic matter enrichment under arid climatic conditions. On the one hand, the blooms of algae and plankton caused high productivity in the surface water, while due to the stable anoxic conditions, the bottom water provided ideal conditions for the preservation of organic matter. On the other hand, under arid climatic conditions, the input of freshwater, detrital minerals and organic matter was significantly reduced, which facilitated water column stratification and contributed to the high burial rate of organic matter. In addition, consumption of $CO_2$ by the algal blooms caused carbonate precipitation, forming the typical carbonate laminae that are associated with the oil shale.

# Acknowledgments

This research was supported by the National Natural Science Foundation of China (41690134, 41821002), the Shandong Provincial Key Research and Development Program (2020ZLYS08), and the Independent innovation research program of China University of Petroleum (East China) (21CX06001A). The project was sup-ported by the Fundamental Research Fundsfor National University, China University of

Geosciences (Wuhan). We thank two anonymous reviewers for helpful comments on the manuscript.

# References

Ackleson, S., Balch., W.M., Holligan, P.M., 1988. White waters of the Gulf of Maine. Oceanography. 1(2):18-22.

Algeo, T.J., Maynard, J.B., 2004. Trace-element behavior and redox facies in core shales of Upper Pennsylvanian Kansas-type cyclothems. Chem. Geol. 206, 289–318.

Algeo, T.J., Rowe, H., 2012. Paleoceanographic applications of trace-metal concentration data. Chem. Geol. 324–325, 6–18.

Algeo, T.J., Li, C., 2020. Redox classification and calibration of redox thresholds in sedimentary systems. Geochimica et Cosmochimica Acta, 287:8-26.

Algeo, T.J., Liu, J.S., 2020. A re-assessment of elemental proxies for paleoredox analysis. Chem. Geol. 540:119549.

Anadon, P., Cabrera, L., Kelts, K., 1991. Lacustrine facies analysis. Blackwell Scientific Publications.

Anderson, R.Y., Dean, W.E., 1988. Lacustrine varve formation through time. Palaeogeogr. Palaeoclimatol. Palaeoecol. 62, 215–235.

Anschutz P., Zhong S., Sundby B., Mucci A. and Gobeil C. 1998. Burial efficiency of phosphorus and the geochemistry of iron in continental margin sediments. Limnol. Oceanogr. 43, 53–64.

Bai, Y.Y., Lv, Q.T., Liu, Z.J., Simon, C. G., Sun, P.C., Meng, Q.T., Xie, W.Q., Song, Q.L., Wang, J.X., Xu, C., 2020. An Analysis of Sedimentary Organic Facies in the Coal-bearing Member of Middle Jurassic Shimengou Formation, Yuqia Area, Qaidam Basin. Acta Geoscientica Sinica. (In Chinese with English Abstruct).

Bahlburg, H., Dobrzinski, N., 2011. A review of the Chemical Index of Alteration (CIA) and its application to the study of Neoproterozoic glacial deposits and climate transitions. In: E. Arnaud, G.P. Halverson, G. Shields-Zhou, The Geological Record of Neoproterozoic Glaciations. Geological Society, London, pp. 81-92.

Behar, F., Beaumont, V., Penteado, H.L., De, B., 2001. Rock-Eval 6 technology: performances and developments. Oil Gas Sci. Technol. Rev. IFP 56, 111–134.

Bohacs, K.M., Carroll, A.R., Neal, J.E.,Mankiewicz, P.J., 2000. Lake-basin type, source potential, and hydrocarbon character: an integrated sequence-stratigraphic-geochemical framework. In: Gierlowski-Kordesch, E.H., Kelts, K.R. (Eds.), Lake Basins Through Space and Time 46. AAPG Studies in Geology, pp. 3–34.

Benitez-Nelson, C.R., 2000. The biogeochemical cycling of phosphorus in marine systems.Earth Sci. Rev. 51 (1–4), 109–135.

Bowen, H.J.M., 1982. Environmental Chemistry. Vol. 2. Royal Society of Chemistry, London, pp. 286.

Burton,D., Woolf, K., Sullivan, B., 2014. Lacustrine depositional environments in the Green River Formation, Uinta Basin: expression in outcrop and wireline logs. AAPG Bull. 98, 1699–1715.

Calvert, S.E., Pedersen, T.F., 1993. Geochemistry of Recent oxic and anoxic marine sediments:

implications for the geological record. Mar. Geol. 113 (1), 67–88.

Canfield, D. E., 1994. Factors influencing organic carbon preservation in marine sediments. Chemical Geology. 114(3-4):315-329.

Carroll, A.R., Bohacs, K.M., 1999. Stratigraphic classification of ancient lakes: balancing tectonic and climatic controls. Geology 27, 99–102.

Carroll, A.R., Bohacs, K.M., 2001. Lake-type controls on petroleum source rock potential in nonmarine basins. AAPG Bull. 85, 1033–1053.

Chaillou, G., Anschutz, P., Lavaux, G., Schäfer, J., Blanc, G., 2002. The distribution of Mo, U, and Cd in relation to major redox species in muddy sediments of the Bay of Biscay. Mar. Chem. 80, 41–59.

Chalmers, G.R.L., Bustin, R.M., 2008. Lower Cretaceous gas shales in northeastern British Columbia, Part I: geological controls on methane sorption capacity. Bulletin of Canadian Petroleum Geology, 56, 1-21.

Chamberlain, C.P.,Wan, X., Graham, S.A., Carroll, A.R., Doebbert, A.C., Sageman, B.B., Peter, B., Malinda, L.K., Zhou,W., Chengshan, W., 2013. Stable isotopic evidence for climate and basin evolution of the Late Cretaceous Songliao basin, China. Palaeogeogr. Palaeoclimatol. Palaeoecol. 385, 106–124.

Chen, L.L., Meng, Q.T., Liu, Z.J., Xu, Y.B., Sun, C.P., Wang, K.B., 2018. Depositional Environment of Coal and Oil Shale of Middle Jurassic Shimengou Formation in Tuanyushan Area, Qaidam Basin. Xinjiang Petroleum Geology. 39(06), 21-30. (In Chinese with English Abstract)

Chen, X. H., G. Gehrels, A. Yin, L. Li, and R. B. Jiang, 2012, Paleozoic and Mesozoic basement magmatisms of eastern Qaidam basin, northern Qinghai–Tibet plateau: LA–ICP–MS zircon U–Pb geochronology and its geological significance: Acta Geologica Sinica (English Edition), 86:350–369.

Chen, Z.Y., Chen, Z.L., Zhang, W.G., 1997. Quaternary stratigraphy and trace-element indices of the Yangtze Delta, Eastern China, with special reference to marine transgressions. Quat. Res. 47 (2), 181–191.

Couch, E.L., 1971. Calculation of paleosalinities from boron and clay mineral data. Am. Assoc. Pet. Geol. Bull. 55 (10), 1829–1837.

Cullers, R.L., Podkovyrov, V.N., 2002. The source and origin of terrigenous sedimentary rocks in the Mesoproterozoic Ui group, southeastern Russia. Precambrian Res. 117 (3–4), 157–183.

Dean, W.E., Gardner, J.V., Piper, D.Z., 1997. Inorganic geochemical indicators of glacialinterglacial changes in productivity and anoxia on the California continental margin. Geochem. Cosmochim. Acta 61 (21), 4507–4518.

Dean, W.E., 1999. The carbon cycle and biogeochemical dynamics in lake sediments. Journal of palaeoclimates. 21(4):375-393.

Deng, H.W., Qian, K., 1993. Elemental geochemistry. In: Deng, H.W., Qian, K. (Eds.), Sedimentary Geochemistry and Environment Analysis. Science and Technology of Gansu Press. Lanzhou, China, pp. 4–31.

Didyk, B.M., Simoneit, B.R.T., Brassell, S.C., Eglinton, G., 1978. Organic geochemical indicators of palaeoenvironmental conditions of sedimentation. Nature 272(5650): 216-222.

Doebbert, A.C., Carroll, A.R., Mulch, A., Chetel, L.M., Chamberlain, C.P., 2010. Geomorphic controls on lacustrine isotopic compositions: evidence from the Laney Member, Green River Formation, Wyoming. Geol. Soc. Am. Bull. 122, 236–252.

Fedo, C.M., Nesbitt, H.W., Young, G.M., 1995. Unraveling the effects of potassium metasomatism in sedimentary rocks and paleosols, with implications for paleoweathering conditions and provenance. Geology 23(10): 921-924.

Froelich P.N., Arthur M.A., Burnett W.C., Deakin M., Hensley V., Jahnke R., Kaul L., Kim K.H., Roe K., Soutar A. and Vathakanon C. 1988. Early diagenesis of organic matter in Peru continental margin sediments: phosphorite precipitation. Mar. Geol. 80, 309–343.

Ghassal, B.I., Littke, R., El Atfy, H., Sindern, S., Scholtysik, G., El Beialy, S., El Khoriby, E., 2018. Source rock potential and depositional environment of Upper Cretaceous sedimentary rocks, Abu Gharadig Basin, Western Desert, Egypt: An integrated palynological, organic and inorganic geochemical study. Int. J. Coal Geol. 186: 14-40.

Guo, T., Ren, S., Luo, X., Bao, S., Wang, S., Zhou, Z., Chen, X., Li, H., Xu, Q., 2018. Accumulation conditions and prospective areas of shale gas in the Middle Jurassic Dameigou Formation, northern Qaidam Basin, Northwest China. Geol. J. 53: 1-11.

Hao, F., Zhou, X., Zhu, Y., Yang, Y., 2011. Lacustrine source rock deposition in response to co-evolution of environments and organisms controlled by tectonic subsidence and climate, Bohai Bay Basin, China. Org. Geochem. 42, 323–339.

Hao, F., Zou, H., Lu, Y., 2013. Mechanisms of shale gas storage: Implications for shale gas exploration in China. AAPG Bull. 97(8): 1325-1346.

Hu, J.J., Ma, Y.S., Wang, Z.X., Liu, Y. Q., Gao, W.L., Qian, T., 2017. Palaeoenvironment and palaeoclimate of the Middle to Late Jurassic revealed by geochemical records in northern margin of Qaidam Basin. Journal of Palaeogeography. 19(3):48-49.

Hu, J.J, Ma, Y.S., Li, Z.X., Wu, Y., Gao, W.L., Peng, B., Wei, X.J., Liu, D. 2019. Jurassic sediments geochemical constraints on provenance, weathering process, and palaeoclimate variation of the north margin of Qaidam Basin, north-eastern Tibetan Plateau. Geological Journal. https://doi.org/10.1002/gj.3542

Hughes, W.B., Holba, A.G., Dzou, L.I.P., 1995. The ratios of dibenzothiophene to phenanthrene and pristane to phytane as indicators of depositional environment and lithology of petroleum source rocks. Geochim. Cosmochim. Ac. 59(17): 3581-3598.

Ingall E. D. and Jahnke R. 1994. Evidence for enhanced phosphorus regeneration from marine sediments overlain by oxygen depleted waters. Geochim. Cosmochim. Acta 58, 2571–2575.

Ingall E. D. and Jahnke R. 1997. Influence of water-column anoxia on the elemental fractionation of carbon and phosphorus during sediment diagenesis. Mar. Geol. 139, 219–229.

Jiang, Z., Chen, D., Qiu, L., Liang, H., Ma, J., 2007. Source-controlled carbonates in a small Eocene half-graben lake basin (Shulu Sag) in central Hebei Province, North China. Sedimentology 54, 265–292.

Jin, Q., Zhu, G.Y. 2006. Progress in research of deposition of oil source rocks in saline lakes and their hydrocarbon generation. Geological Journal of China Universities, 16(16):511-524.

Johnson Ibach, L.E., 1982. Relationship between sedimentation rate and total organic carbon content in ancient marine sediments. AAPG Bull. 66, 170–188.

Kang, Z., Zhou, L., Ren, S., Kong, J., Chen, Y., 2015. Characteristics of shale of the 7th member of the Middle Jurassic Dameigou Formation in Northern Qaidam Basin. Earth Science Frontiers 22(4): 265-276.

Katz, B.J., 1990. Controls on distribution of lacustrine source rocks through time and space. In: Katz, B.J. (Ed.), Lacustrine Basin Exploration-case Studies and Modern Analogs. AAPG (Tulsa) Mem. 50, 61-76.

Katz, B., Lin, F., 2014. Lacustrine basin unconventional resource plays: key differences. Mar. Pet. Geol. 56, 255–265.

Katz, B.J., Liu, Xingcai, 1998. Summary of the AAPG Research Symposium on lacustrine basin exploration in China and Southeast Asia. AAPG Bull. 82, 1300-1307.

Kendall, B., Reinhard, C.T., Lyons, T.W., Kaufman, A.J., Poulton, S.W., Anbar, A.D., 2010. Pervasive oxygenation along late Archaean ocean margins, Nature Geoscience, 3, 647-652.

Kent-Corson, M.L.,Mulch, A., Graham, S.A., Carroll, A.R., Ritts, B.D., Chamberlain, C.P., 2010. Diachronous isotopic and sedimentary responses to topographic change as indicators of mid-Eocene hydrologic reorganization in the western United States. Basin Res. 22, 829–845.

Kemp, A. E. S., 1996. Paleoclimatology and paleoceanography from laminated sediments. London: Geological Society Special Publication. 50:1583-1591.

Kidder, G., Brown, R.B., Littell, R., 1996. Phosphorus retention as related to morphology of sandy coastal plain soil materials. Soil Sci. Soc. Am. J. 60 (5), 1513–1521.

Krauskopf, K.B., 1956. Factors controlling the concentrations of thirteen rare metals in sea-water. Geochim. Cosmochim. Acta 9 (1–2), B1–B32.

Krom, M.D., Berner R.A., 1981. The diagenesis of phosphorus in a nearshore marine sediment. Geochim. Cosmochim. Acta. 45, 207–216.

Lallier, V.E., Hayes, J.M., Boussafir, M., 1996. Productivity-induced sulphur enrichment of hydrocarbon-rich sediments from the Kimmeridge Clay Formation. Chemical Geology. 134 :277-288.

Lan, X.H., Ma, D.X., Xu, M.G., Zhou, Q.W., Zhang, G.W., 1987. Some geochemical indicators of the Pearl River Delta and their facies significance. Marine Geol. Quat. Geol. 7 (1), 39–49.

Lerman, A., Imboden, D.M., Gat, J., Chou, L., 1995. Physics and Chemistry of Lakes. Springer-Verlag, Physics and chemistry of lakes. Springer-Verlag.

Li, D.S., Jiang, R.Q., Katz, B.J., 1995. Petroleum generation in the nonmarine Qingshankou Formation (Lower Cretaceous), Songliao basin, China. In: Katz, B.J. (Ed.), Petroleum Source Rocks. SpringereVerlag, Heidelberg, pp. 131-148.

Li, G.,Wang, Y., Lu, Z., Liao,W., Song, G.,Wang, X., Xu, X., 2014. Geobiological processes of the formation of lacustrine source rock in Paleogene. Sci. China Earth Sci. 57, 976–987.

Li, M., Shao, L., Lu, J., Spiro, B., Wen, H., Li, Y., 2014. Sequence stratigraphy and paleogeography of the Middle Jurassic coal measures in the Yuqia coalfield, northern Qaidam Basin, northwestern China. AAPG Bull. 98(12): 2531-2550.

Li, M., Shao, L.Y., Liu, L., Lu, J., Spiro, B., W, H.J., Li, Y.H., 2016. Lacustrine basin evolution and coal accumulation of the Middle Jurassic in the Saishiteng coalfield, northern Qaidam Basin, China. Journal of Palaeogeography, 5(3):205-220.

Liu, B., Lv, Y.F., Meng, Y.L., Li, X.N., Guo, X.B., Ma, Qaing., Zhao, W.C. 2015. Petrologic characteristics and genetic model of lacustrine lamellar fine-grained rock and its significance for shale oil exploration: A case study of Permian Lucaogou Formation in Malang sag, Santanghu Basin, NW China. 42(5):598-607.

Liu, T. Y., Hu, K., Cao, J., Yang, S.Y., B, L.Z., W, L.Q., Chen, D., 2008. Organic biofacies of Jurassic source rocks in northern Qaidam Basin, NW China. Petroleum Exploration and Development.

035(003):281-288.

Nameroff, T.J., Balistrieri, L.S., Murray, J.W., 2002. Suboxic trace metal geochemistry in the eastern tropical north pacific. Geochem. Cosmochim. Acta 66 (7), 1139–1158.

Nesbitt, H.W., Young, G.M., 1982. Early Proterozoic climates and plate motions inferred from major element chemistry of lutites. Nature 299(5885): 715-717.

Neumann, V.H., Borrego, A.G., Cabrera, L., Dino, R., 2003. Organic matter composition and distribution through the Aptian–Albian lacustrine sequences of the Araripe Basin, northeastern Brazil. Int. J. Coal Geol. 54, 21–40.

Macquaker, J.H., Bohacs, K.M., 2007. On the accumulation of mud. Science 318, 1734–1735.

Macquaker, J.H., Keller, M.A., Davies, S.J., 2010. Algal blooms and “marine snow”: mechanisms that enhance preservation of organic carbon in ancient fine-grained sediments. J. Sediment. Res. 80, 934–942.

Ma, Y.Q., Fan M.J., Lu, Y.C., Liu, H.M., Hao, Y.Q., Xie, Z.H., Liu, Z.H., Li, P., Du, X.B., Hu, H.Y., 2016. Climate-driven paleolimnological change controls lacustrine mudstone depositional process and organic matter accumulation: Constraints from lithofacies and geochemical studies in the Zhanhua Depression, eastern China. Int. J. Coal Geol. 167:103-118.

Mclennan, S.M., 1993. Weathering and Global Denudation. J. Geol. 101(2): 295-303.

Mei, B., Liu, X., 1980. The distribution of isoprenoid alkanes in China’s crude oil and its relation with the geologic environment. Oil and Gas Geology 1(2): 99-115.

Meng, Q.T., Liu, Z.J., Sun P.C., Xu, Y.B., Li, F., Bai, Y.Y., Xie, W.Q., Dong, S., Song, S., Wang, K.B., Xu, C., 2018. Characteristics and accumulation of middle jurassic oil shale in the Yuqia area, northern Qaidam Basin, Northwest China. Oil Shale, 35(1):1-25.

Meng, Q. T., Bechtel, A., Sachsenhofer, R. F., Liu, Z.J., Gross, D., Sun, P.C., 2019. Hydrocarbon potential and palaeo ő epositional environment of lacustrine source rocks: middle jurassic shimengou formation, northern qaidam basin, nw china. Journal of Petroleum Geology, 42(1), 37-58.

McManus, J., Berelson, W.M., Klinkhammer, G.P., Hammond, D.E., Holm, C., 2005. Authigenic uranium: relationship to oxygen penetration depth and organic carbon rain. Geochim. Cosmochim. Acta 69, 95–108.

Meyers, P.A., 1997. Organic geochemical proxies of paleoceanographic, paleolimnologic, and paleoclimatic processes. Organic Geochemistry, 27(5-6): 213-250.

Morford, J.L., Emerson, S.T., 1999. The geochemistry of redox sensitive trace metals in sediments. Geochim. Cosmochim .Acta. 63(12):1735-1750.

Nara, F., Tani, Y., Soma, Y., Soma, M., Naraoka, H., Watanabe, T., Horiuchi, K., Kawai, T., Oda, T., Nakamura, T., 2005. Response of phytoplankton productivity to climate change recorded by sedimentary photosynthetic pigments in Lake Hovsgol (Mongolia) for the last 23,000 years. Quaternary International, 136(1), 71—81.

Pais, I., Jones, J.B. 1997. The Handbook of Trace Elements, 1st ed. St. Lucie Press, Boca Raton, Florida, p. 225.

Pattan, J.N., Pearce, N.J.G., Mislankar, P.G., 2005. Constraints in using Cerium-anomaly of bulk sediments as an indicator of paleo bottom water redox environment: A case study from the Central Indian Ocean Basin. Chem. Geol. 221:260-278.

Peters, K.E., Walters, C.C., Moldowan, J.M., 2005. The biomarker guide. Cambridge University Press.

Piper, D.Z., Perkins, R.B., 2004. A modern vs. Permian black shale—the hydrography, primary productivity, and water-column chemistry of deposition. Chem. Geol. 206 (3–4), 177–197.

Poulton, S.W., Raiswell, R., 2002. The low-temperature geochemical cycle of iron: from continental fluxes to marine sediment deposition. American Journal of Science, 302(9).

Qian, T., Wang, Z. X., Liu, Y. Q., Liu, S. F., Gao, W. L., Li, W. P., Li, L. L., 2018. Provenance analysis of the Jurassic northern Qaidam Basin: Stratigraphic succession and LA-ICP-MS geochronology. Scientia Sinica Terrae, 48(2), 224-242.

Qin, J., Wang, S.Q., Sanei, H., Jiang, C.Q., Chen, Z.H., Ren, S.M., Xu, X.M., Yang, J.J., Zhong, N.N., 2018. Revelation of organic matter sources and sedimentary environment characteristics for shale gas formation by petrographic analysis of middle Jurassic Dameigou formation, northern Qaidam Basin, China. Int. J. Coal Geol. 195:373-385.

Berner, R.A., Raiswell, R., 1984. C/S method for distinguishing freshwater from marine sedimentary rocks. Geology. 12, 365-368.

Reheis, M.C., 1990. Influence of climate and eolian dust on the major-element chemistry and clay mineralogy of soils in the northern Bighorn Basin, U.S.A. Catena 17 (3), 219–248.

Ren, Y., Chen, D., Kelsey, D.E., Gong, X., Liu, L., 2017. Petrology and Geochemistry of the lawsonite (pseudomorph)-bearing eclogite in Yuka terrane, North Qaidam UHPM belt: An eclogite facies metamorphosed oceanic slice. Gondwana Res. 42: 220-242.

Rimmer, S.M., 2004. Geochemical paleoredox indicators in devonian–mississippian black shales, central appalachian basin (USA). Chem. Geol. 206 (3–4), 373–391.

Ritts, B. D., Hanson, A. D., Zinniker, D., Moldowan, J. M. 1999. Lower-Middle Jurassic nonmarine source rocks and petroleum systems of the northern Qaidam basin, northwest China. AAPG bulletin, 83(12), 1980-2005.

Ritts, B. D., & Biffi, U. 2001. Mesozoic northeast Qaidam basin: Response to contractional reactivation of the Qilian Shan, and implications for the extent of Mesozoic intracontinental deformation in central Asia. Memoirs-Geological Society of America, 293-316.

Sageman, B.B., Murphy, A.E., Werne, J.P., Ver Straeten, C.A., Hollander, D.J., Lyons, T.W., 2003. A tale of shales: the relative roles of production, decomposition, and dilution in the accumulation of organic-rich strata, Middle–Upper Devonian, Appalachian basin. Chem. Geol. 195 (1–4), 229–273.

Salminen, R., Batista, M.J., Bidovec, M., Demetriades, A., De Vivo, B., De Vos, W., 2005. FOREGS Geochemical Atlas of Europe, Part I: Background Information, Methodology,and Maps. Geological Survey of Finland, Espoo.

Shang, X., Shao, L., Zhang, W., Lv, J., Wang, W., Li, Y., Wen, H. 2018. Sequence paleogeography and coal accumulation of the Early-Middle Jurassic in central Qilian Mountain belt (Muli Basin), Qinghai Province, northwestern China. AAPG Bulletin, 102(9), 1739-1762.

Schoepfer, S.D., Shen, J., Wei, H.Y., Tyson, R.V., Ingall, E., Algeo, T.J., 2015. Total organic carbon, organic phosphorus, and biogenic barium fluxes as proxies for paleomarine productivity. Earth Sci. Rev. 149, 23–52.

Scholle, P.A., Bebout, D.G. and Moore, C.H. 1983. Carbonate Depositional Environments. AAPG Memoir, 33:297-343.

Shao, L.Y., Li, M., Li, Y.H., Zhang, Y.P., Lu, J., Zhang, W.L., Tian, Z., Wen, H.J., 2014. Geological characteristics and controlling factors of shale gas in Jurassic of northern Qaidam Basin. Earth Science Frontiers. 21(4):311-322.

Slomp C.P., Epping E.H.G., Helder W. and van Raaphorst W. 1996a. A key role for iron-bound phosphorus in authigenic apatite formation in North Atlantic continental platform sediments. J. Mar. Res. 54, 1179–1205.

Slomp C.P., Van der Gaast S. J. and van Raaphorst W. 1996b. Phosphorus binding by poorly crystalline iron oxides in North Sea sediments. Mar. Chem. 52, 55–73.

Slomp C. P., Thompson J. and de Lange G. J. 2002. Enhanced regeneration of phosphorus during formation of the most recent eastern Mediterranean sapropel (S1). Geochim. Cosmochim. Acta 66, 1171–1184.

Slomp C. P., Thomson J. and de Lange G. J. 2004. Controls on phosphorus regeneration and burial during formation of eastern Mediterranean sapropels. Mar. Geol. 203, 141–159.

Smith, M.E., Carroll, A.R., Mueller, E.R., 2008. Elevated weathering rates in the Rocky Mountains during the early Eocene climatic optimum. Nat. Geosci. 1, 370–374.

Smith, M.E., Carroll, A.R., Scott, J.J., 2015. Stratigraphic expression of climate, tectonism, and geomorphic forcing in an underfilled lake basin: Wilkins Peak Member of the Green River Formation. In: Smith, M.E., Carroll, A.R. (Eds.), Stratigraphy and Paleolimnology of the Green River Formation. Western USA. Springer, Dordrecht, pp. 61–102.

Song, Y., Li, S.F., Hu, S.Z., 2019. Warm-humid paleoclimate control of salinized lacustrine organic-rich shale deposition in the Oligocene Hetaoyuan Formation of the Biyang Depression, East China. Int. J. Coal Geol. 202:69-84.

Tissot, B.P., Welte, D.H., 1984. Petroleum Formation and Occurrence. Springer Berlin Heidelberg.

Tribovillard, N., Algeo, T.J., Lyons, T., Riboulleau, A., 2006. Trace metals as paleoredox and paleoproductivity proxies: an update. Chem. Geol. 232 (1–2), 12–32.

Van Cappellen P. and Ingall E. D. 1994. Benthic phosphorus regeneration, net primary production, and ocean anoxia: A model of the coupled marine biogeochemical cycles of carbon and phosphorus. Paleoceanography 9, 677–692.

Waples, D.W., Machihara, T., 1990. Application of sterane and triterpane biomarkers in petroleum exploration. Bulletin of Canadian Petroleum Geology 38(3): 357-380.

Wang, G.M., Zhong, J.H. 2004. A review and the prospects of the researches on sedimentary mechanism of lacustrine laminae. Acta Petrologica Et Mineralogica. 23(1):43-48.

Wang, G.M., 2012 Laminae Combination and Genetic Classification of Eogene Shale in Jiyang Depression. Journal of Jilin University. 42(3): 666-671.

Wang, J. C., Y. Hu, and Y. T. Liu, 2006, Control of multigeneration rotary normal faults on sediment migration in rift basin: An example from the Early and Middle Jurassic Qaidam Basin: Acta Geologica Sinica. 80:1141–1148.

Wang, L., Yu, Q.C., 2016. The effect of moisture on the methane adsorption capacity of shales: A study case in the eastern Qaidam Basin in China. Journal of Hydrology. 542:487-505.

Wang, T., Yang, S., Duan, S., Chen, H., Liu, H., Cao, J., 2015. Multi-stage primary and secondary hydrocarbon migration and accumulation in lacustrine Jurassic petroleum systems in the northern Qaidam Basin, NW China. Mar. Petrol. Geol. 62: 90-101.

Wang Y.D., Mosbrugger, V., Zhang, H., 2005. Early-Middle Jurassic vegetation and climate events in the Qaidam Basin, China. Palaeogeography, Palaeoclimatology, Palaeoecology, 224: 200-216.

Wang, Y.X., Xu, S., Hao, F., Lu, Y.B., Shu, Z.G., Yan, D.T., Lu, Y.C., 2019. Geochemical and petrographic characteristics of Wufeng-Longmaxi shales, Jiaoshiba area, southwest China:

Implication for organic matter differential accumulation. Mar. Pet. Geol. 102, 138–154.

Wang, Y.X., Xu, S., Hao, F., Zhang, B.Q., Shu, Z.G., Gou, Q.Y., Lu, Y.B., Cong, F.Y., 2020. Multiscale petrographic heterogeneity and their implications for the nanoporous system of the Wufeng Longmaxi shales in Jiaoshiba area, Southeast China: Response to depositional-diagenetic process. Geol. Soc. Am. Bull. 132 (7-8): 1704–1721.

Wei, W., Algeo, T. J., Lu, Y., Lu, Y., Liu, H., Zhang, S., Peng, L., Zhang, J. and Chen, L., 2018. Identifying marine incursions into the Paleogene Bohai Bay Basin lake system in northeastern China. Int. J. Coal Geol. 200, 1–17.

Wei, W., Algeo, T. J., 2019. Elemental proxies for paleosalinity analysis of ancient shales and mudrocks. Geochim. Cosmochim. Acta. Inpress.

Xiong, Y.J., Guilbaud, R., Peacock, C. L., Cox, R. P., Poulton, S.W., 2019. Phosphorus cycling in lake cadagno, switzerland: a low sulfate euxinic ocean analogue. Geochimica et Cosmochimica Acta, 251.

Yang, S.Y., Li, C.X., Yang, D.Y., Li, X.S., 2004a. Chemicalweathering of the loess deposits in the lower Changjiang Valley,China, and paleoclimatic implications. Quat. Int. 117(1), 27–34.

Yang, S.Y., Jung, H.S., Li, C., 2004b. Two unique weatheringregimes in the Changjiang and Huanghe drainage Basins:geochemical evidence from river sediments. Sed. Geol. 164(1),19–34.

Yang, Y.T., Zhang B.M., Zhao, C.Y., Xu, T.G., 2004. Mesozoic source rocks and petroleum systems of the northeastern Qaidam basin, northwest China. AAPG Bull. 88(1): 115-125.

Yang, Z., Zou, C.N., Wu, S.T., Lin, H.S., Pan, S.Q., Niu, X.B., Men, G.T., Tang, Z.X., Li, G.H., Zhao, J.H., Jia, X.Y., 2019. Formation, distribution and resource potential of the "sweet areas (sections)" of continental shale oil in China. Mar. Pet. Geol. 102, 48–60.

Young, G.M., Nesbitt, H., 1999. Paleoclimatology and provenance of the glaciogenic gowganda formation (paleoproterozoic), ontario, Canada: a chemostratigraphic approach. Geol. Soc. Am. Bull. 111 (2), 264–274.

Zakir Hossain, H.M., Sampei, Y., Roser, B.P., 2009. Characterization of organic matter and depositional environment of Tertiary mudstones from the Sylhet Basin, Bangladesh. Org. Geochem. 40(7): 743-754.

Zhang, X.G., Lin, C., Zahid, M.A., Jia, X., Zhang, T., 2017. Paleosalinity and water body type of Eocene Pinghu Formation, Xihu Depression, East China Sea Basin. J. Pet. Sci. Eng. 158, 469–478.

Zheng, R., Liu, H., 1999. Study on palaeosalinity of Chang-6 oil reservoir set in Ordos Basin. Oil Gas Geol. 20, 20–25.

Zheng, Y., Anderson, R.F., van Geen, A., Fleisheir, M.Q., 2002a. Preservation of non-lithogenic particulate uranium in marine sediments. Geochim. Cosmochim. Acta 66, 3085–3092.

Zheng, Y., Anderson, R.F., van Geen, A., Fleisheir, M.Q., 2002b. Remobilization of authigenic uranium in marine sediments by bioturbation. Geochim. Cosmochim. Acta 66, 1759–1772.

Zeng, W.R., Meng, Q.T., Liu, Z.J., Xu, Y.B., Sun, P.C., Wang, K.B., 2019. Organic Geochemical Characteristic and Paleo-Lake Conditions of Oil Shale of Middle Jurassic Shimengou Formation Area of Northern Qaidam Basin. Journal of Jilin University (Earth Science Edition), 2019, 49(05).(In Chinese with English Abstract).

Zhu, G.Y., Jing, Q., Zhang, S.C., Dai, J.X., Wang, G.M., Zhang, L.Y., Li, J., 2005. Characteristics and origin of deep lake oil shale of the Shahejie Formation of Paleogene in Dongying Sag, Jiyang Depression. 7(1):59-69.

# Figure captions

Figure 1. (A) Location map showing the position of Qaidam Basin in China; (B) Map showing the structural divisions of the Qiadam Basin (modified from Guo et al., 2018); (C) Variations in the thickness and facies within the $J_2d^7$ shales, northern Qaidam Basin (modified from Kang et al., 2015). The location of Chaiye 1 (CY1) is well marked in Fig 1C. Cross-section showing the structural framework of the Yuqia sag (modified from Li et al., 2014).

Figure 2. Generalized stratigraphy of the Middle Jurassic Dameigou Formation in Yuqia area of the northern Qaidam Basin (modified from Li et al., 2015). The target stratum is highlighted. MRS=maximum regressive surface; MFS=maximum flooding surface; SU=subaerial unconformity; HST=highstand systems tract; TST=transgressive systems tract; LST=lowstand systems tract.

Figure 3. Stratigraphic plot showing the lithology and sedimentary structures of the middle Jurassic Dameigou Formation in the CY1 well. Black arrows show the positions of the thin sections, XRD and TOC analyses. Red arrows show the sample positions for major and trace element analyses. Green stars represent locations of core samples for the organic geochemical analyses shown in Fig. 8.

Figure 4. Representative thin sections from the $J_2d^7$ formation in the CY1 well. (A) Sandy mudstone, 1917.5 m, mainly composed of coarse-grained detrital minerals, such as quartz and feldspar; (B) Organic-rich mudstone, 1950.2 m, high organic matter content with abundant fine-grained feldspar, quartz and clay minerals; (C) Oil shale, 1924.2 m, black colored oil shale; (D) Oil shale, 1925.5 m, finely laminated black shale, supporting deposition from anoxic bottom waters; (E) Oil shale, 1926.7 m, fossils of algal residue paralleled distributed with bedings; (F)

Oil shale, 1926.7 m, fossils of algal residue stacked as lenticles; (G) Oil shale, 1927.5m, single algal fossil; (H) Argillaceous mudstone, 1910.2 m, gray and black massive shale, with a high clay content, low organic matter content, and a small proportion of quartz and feldspar.

Figure 5. Temary diagram showing the mineral composition of four major lithofacies in the CY1 well through the $J_2d^7$ formation.

Figure 6. Stratigraphic distribution of lithofacies, organic matter features, and paleoclimate data for samples from the $J_2d^7$ formation in the CY1 well.

Figure 7. Stratigraphic distribution of palaeosalinity, redox conditions, and primary productivity data for the CY1 well samples in the $J_2d^7$ formation.

Figure 8. Organic geochemical data for the $J_2d^7$ formation in the Yuqia area. Colored sample points were collected from the CY1 well (data from Qin et al., 2018). Gray samples were collected from other wells in the Yuqia area (data from Ritt et al., 1999; Guo et al., 2018; Chen et al., 2018; Meng et al., 2018; Meng et al., 2019; Zeng et al., 2019; Bai 2020). (A) Coss-plot of HI and $T_{mas}$ for shales of the $J_2d^7$ formation in the Yuqia area; (B) Ternary diagram of $C_{27}$, $C_{28}$ and $C_{29}$ steranes based on their responses on GC–MS m/z 217 mass chromatograms; (C) Cross-plot of Pr/n-C17 and Ph/n-C18; (D) Cross-plot of GI and Pr/Ph ratios for different shales.

Figure 9. Schematic illustration showing factors controlling oil shale development and the accumulation of organic matter in a lacustrine setting under an arid (A) and humid (B) climate.

# Table Captions

Table 1. Mineral composition (wt.%) and total organic carbon concentrations (TOC wt.%) for the four lithofacies in the $J_2d^7$ formation.

Table 2. Geochemical indexes in CY1 well sanples from the $J_2d^7$ formation.

Figure 1

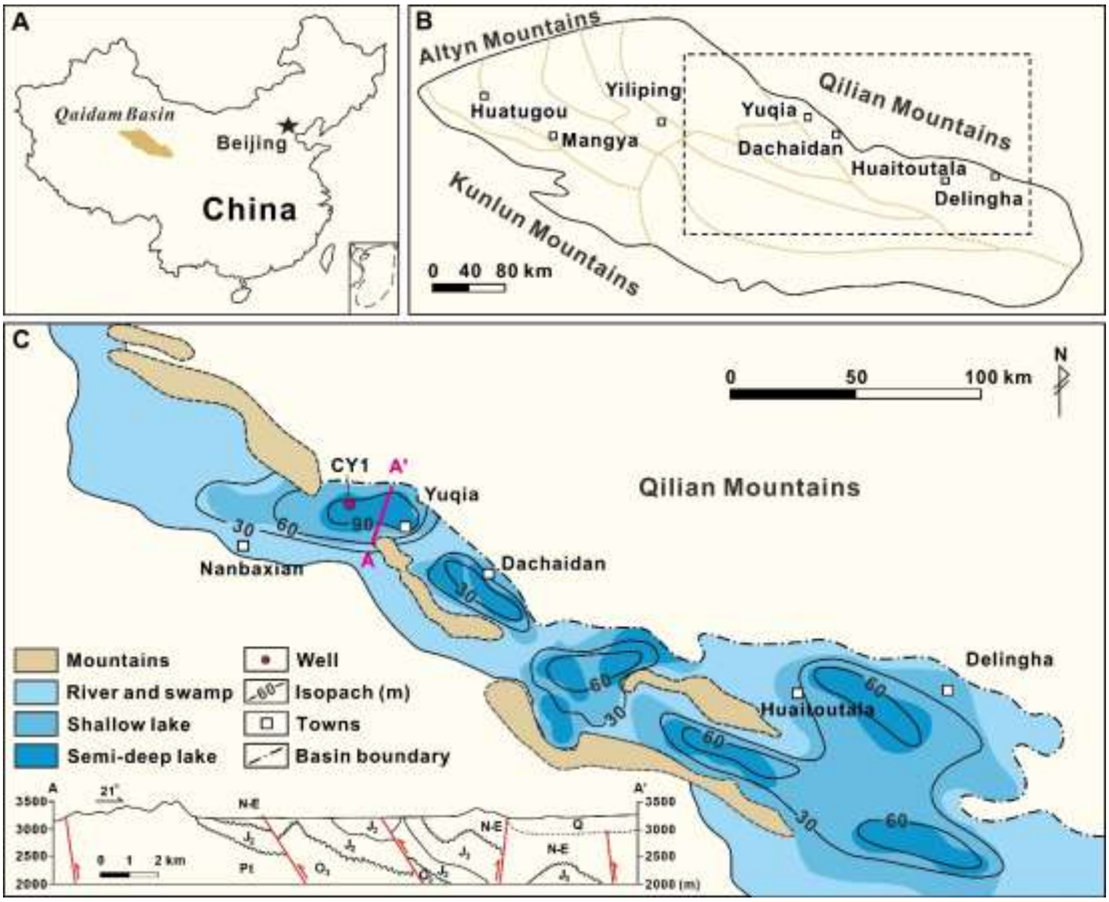
A
Qaidam Basin
Beijing
China
B
Altyn Mountains
Yiliping
Huatugou
Mangya
Qilian Mountains
Yuqia
Dachaidan
Huaitoutala
Delingha
Kunlun Mountains
0 40 80 km
C
0 50 100 km
N
CY1
A'
A
Yuqia
Qilian Mountains
30
60
90
Nanbaxian
Dachaidan
Delingha
Huaitoutala
Mountains
River and swamp
Shallow lake
Semi-deep lake
Well
Isopach (m)
Towns
Basin boundary
3500
3000
2500
2000
0 1 2 km
N-E
Q
Pt
2000 (m)

Figure 2

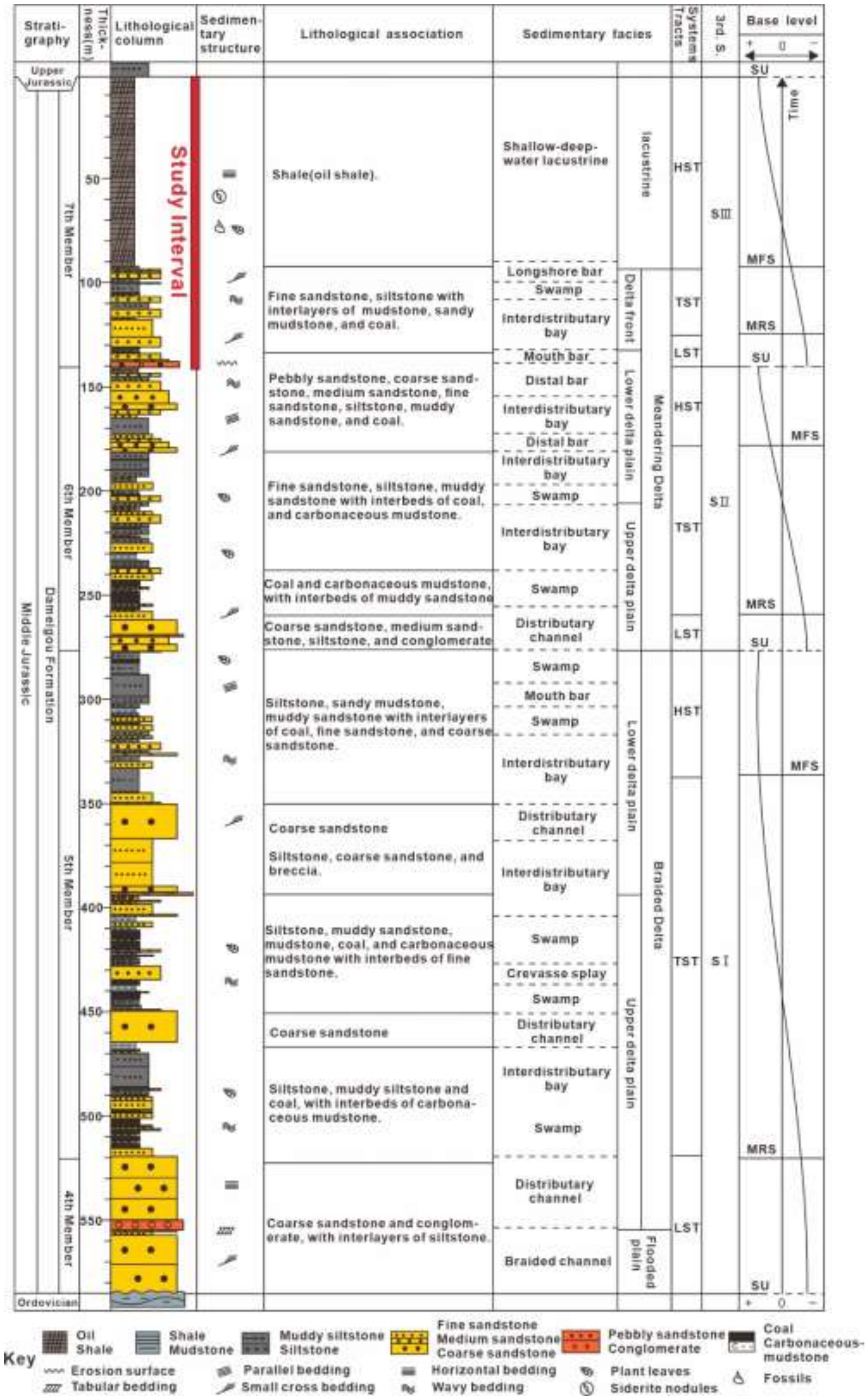

Strati-graphy
Thick-ness(m)
Lithological column
Sedimen-tary structure
Lithological association
Sedimentary facies
Systems Tracts
3rd S.
Base level
Upper Jurassic
Middle Jurassic
Dameigou Formation
7th Member
6th Member
5th Member
4th Member
Ordovician
Study Interval
Shale(oil shale).
Fine sandstone, siltstone with interlayers of mudstone, sandy mudstone, and coal.
Pebbly sandstone, coarse sandstone, medium sandstone, fine sandstone, siltstone, muddy sandstone, and coal.
Fine sandstone, siltstone, muddy sandstone with interbeds of coal, and carbonaceous mudstone.
Coal and carbonaceous mudstone, with interbeds of muddy sandstone
Coarse sandstone, medium sandstone, siltstone, and conglomerate
Siltstone, sandy mudstone, muddy sandstone with interlayers of coal, fine sandstone, and coarse sandstone.
Coarse sandstone
Siltstone, coarse sandstone, and breccia.
Siltstone, muddy sandstone, mudstone, coal, and carbonaceous mudstone with interbeds of fine sandstone.
Coarse sandstone
Siltstone, muddy siltstone and coal, with interbeds of carbonaceous mudstone.
Coarse sandstone and conglomerate, with interlayers of siltstone.
Shallow-deep-water lacustrine
Longshore bar
Swamp
Interdistributary bay
Mouth bar
Distal bar
Distributary channel
Crevasse splay
Braided channel
lacustrine
Delta front
Lower delta plain
Upper delta plain
Flooded plain
Meandering Delta
Braided Delta
HST
TST
LST
SⅢ
SⅡ
SⅠ
SU
MFS
MRS
Time
Key
Oil Shale
Shale Mudstone
Muddy siltstone Siltstone
Fine sandstone Medium sandstone Coarse sandstone
Pebbly sandstone Conglomerate
Coal Carbonaceous-mudstone
Erosion surface
Tabular bedding
Parallel bedding
Small cross bedding
Horizontal bedding
Wavy bedding
Plant leaves
Siderite nodules
Fossils

Figure 3

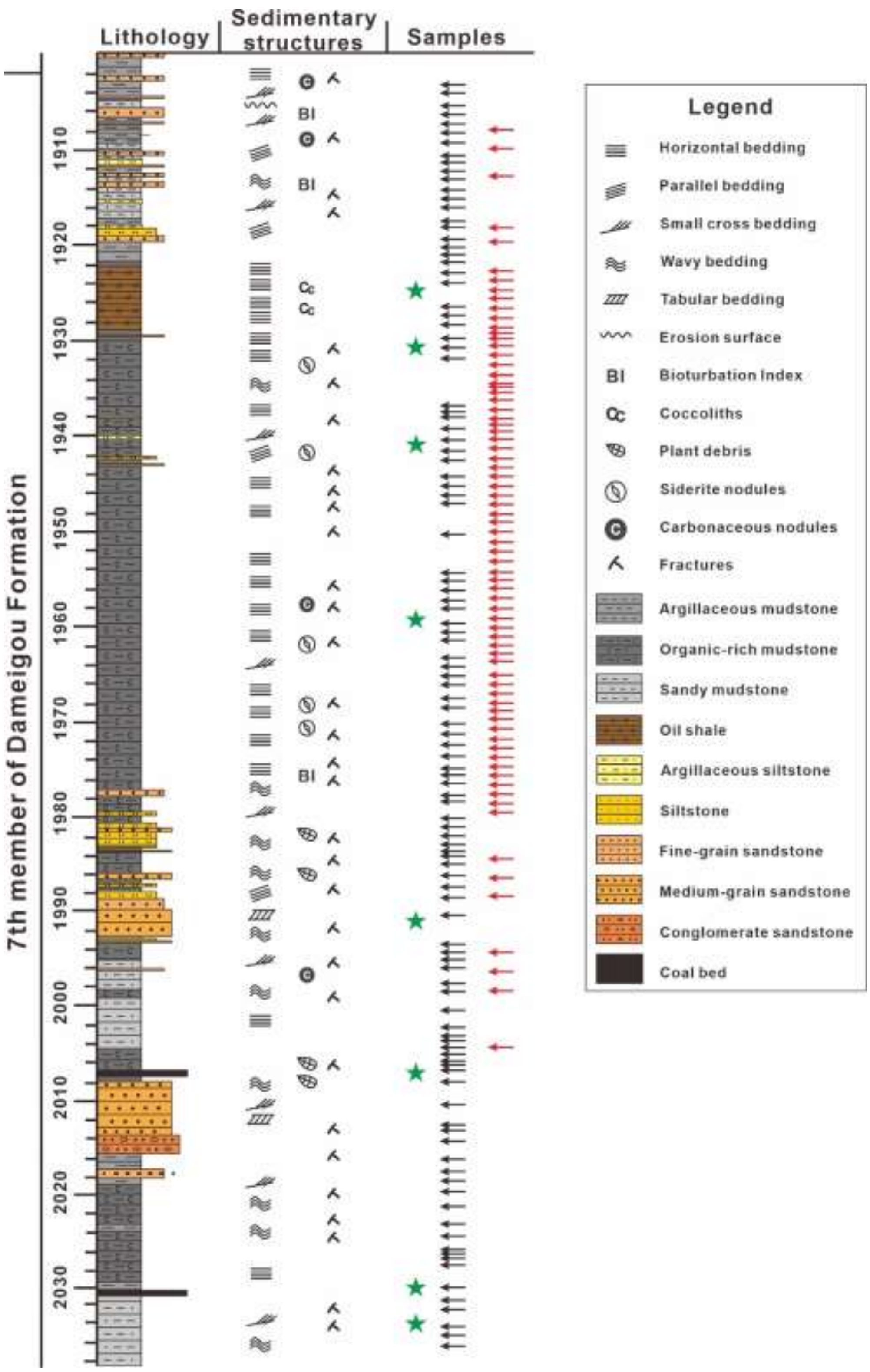

Lithology
Sedimentary structures
Samples
7th member of Dameigou Formation
1910
1920
1930
1940
1950
1960
1970
1980
1990
2000
2010
2020
2030
BI
Cc
Legend
Horizontal bedding
Parallel bedding
Small cross bedding
Wavy bedding
Tabular bedding
Erosion surface
BI
Bioturbation Index
Coccoliths
Plant debris
Siderite nodules
Carbonaceous nodules
Fractures
Argillaceous mudstone
Organic-rich mudstone
Sandy mudstone
Oil shale
Argillaceous siltstone
Siltstone
Fine-grain sandstone
Medium-grain sandstone
Conglomerate sandstone
Coal bed

Figure 4

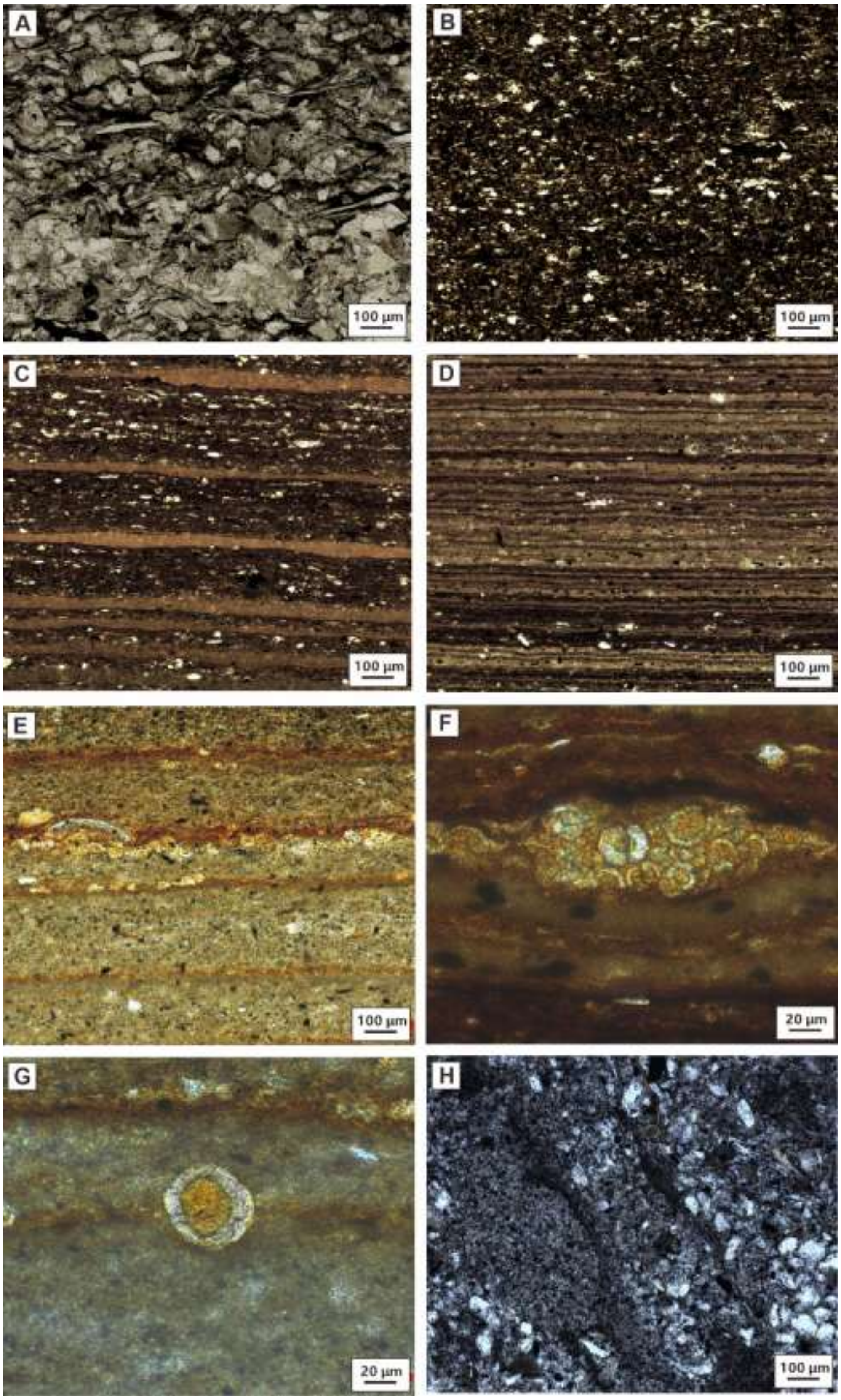

Figure 5

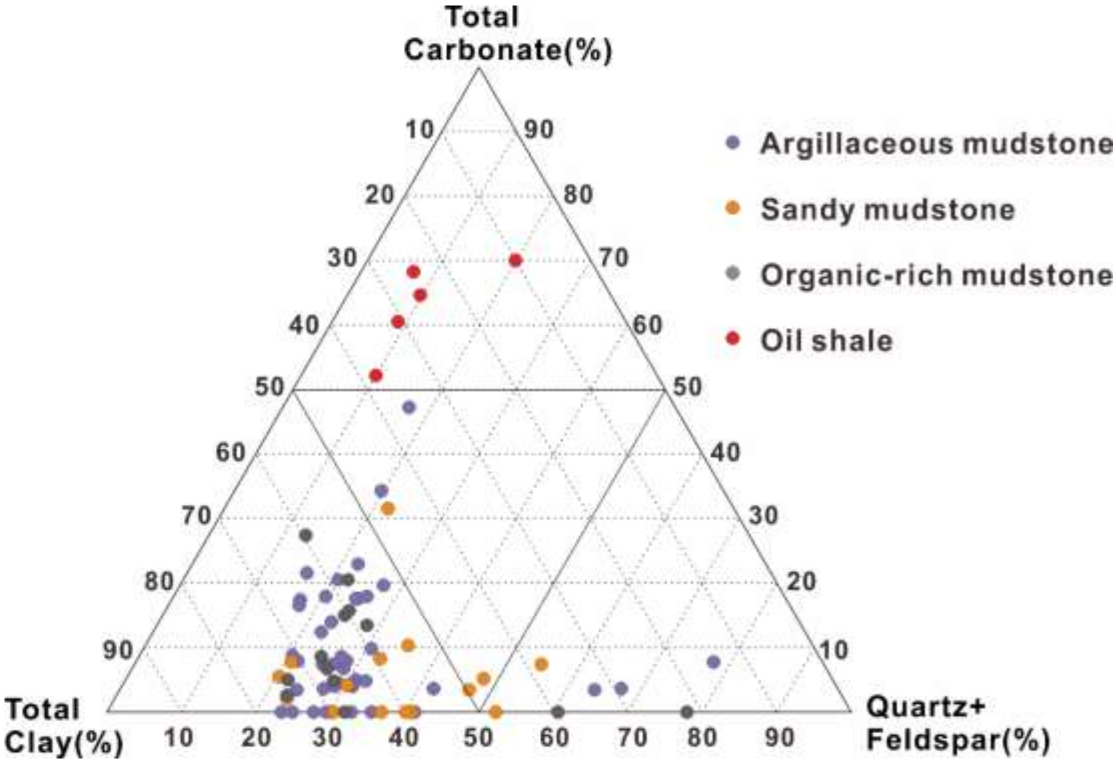
Total Carbonate(%)
Total Clay(%)
Quartz+ Feldspar(%)
Argillaceous mudstone
Sandy mudstone
Organic-rich mudstone
Oil shale
10
20
30
40
50
60
70
80
90

Figure 6

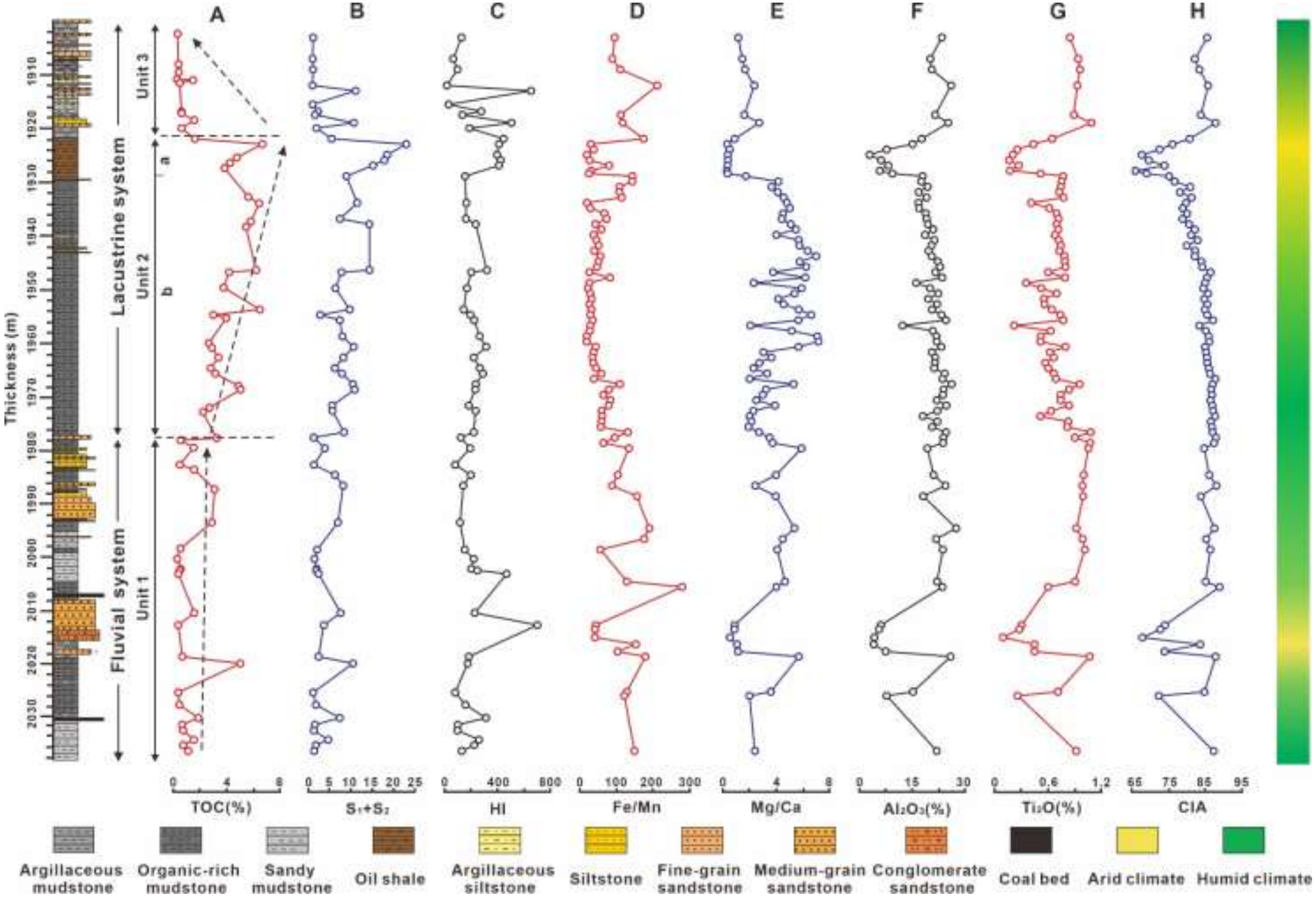
A
B
C
D
E
F
G
H
Thickness (m)
Lacustrine system
Fluvial system
Unit 3
Unit 2
Unit 1
a
b
TOC(%)
S1+S2
HI
Fe/Mn
Mg/Ca
Al2O3(%)
Ti2O(%)
CIA
Argillaceous mudstone
Organic-rich mudstone
Sandy mudstone
Oil shale
Argillaceous siltstone
Siltstone
Fine-grain sandstone
Medium-grain sandstone
Conglomerate sandstone
Coal bed
Arid climate
Humid climate

Figure 7

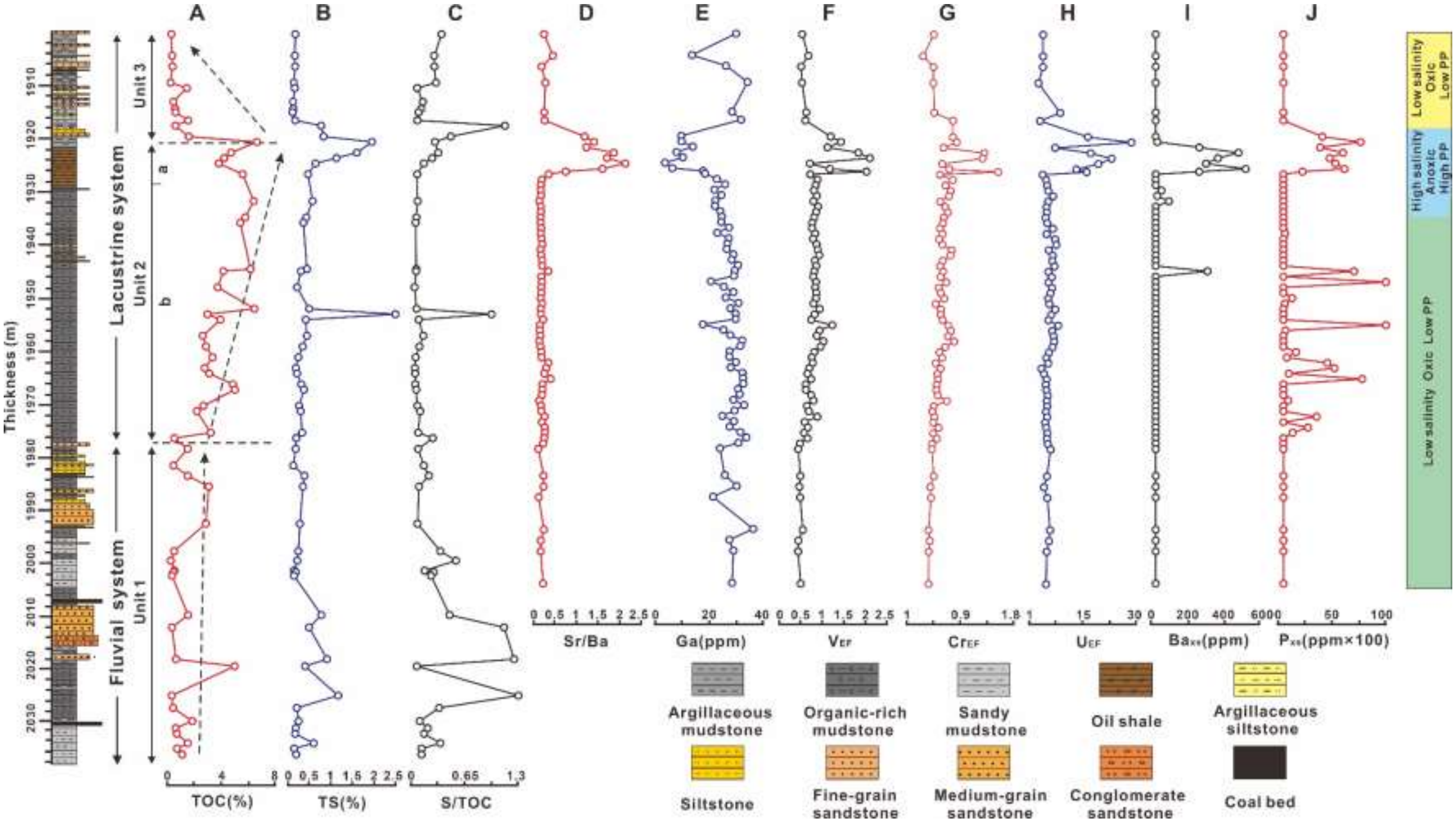
A
B
C
D
E
F
G
H
I
J
Thickness (m)
Lacustrine system
Fluvial system
Unit 3
Unit 2
Unit 1
a
b
TOC(%)
TS(%)
S/TOC
Sr/Ba
Ga(ppm)
VEF
CrEF
UEF
Baxs(ppm)
Pxs(ppm×100)
Low salinity Oxic Low PP
High salinity Anoxic High PP
Low salinity Oxic Low PP
Argillaceous mudstone
Organic-rich mudstone
Sandy mudstone
Oil shale
Argillaceous siltstone
Siltstone
Fine-grain sandstone
Medium-grain sandstone
Conglomerate sandstone
Coal bed

Figure 8

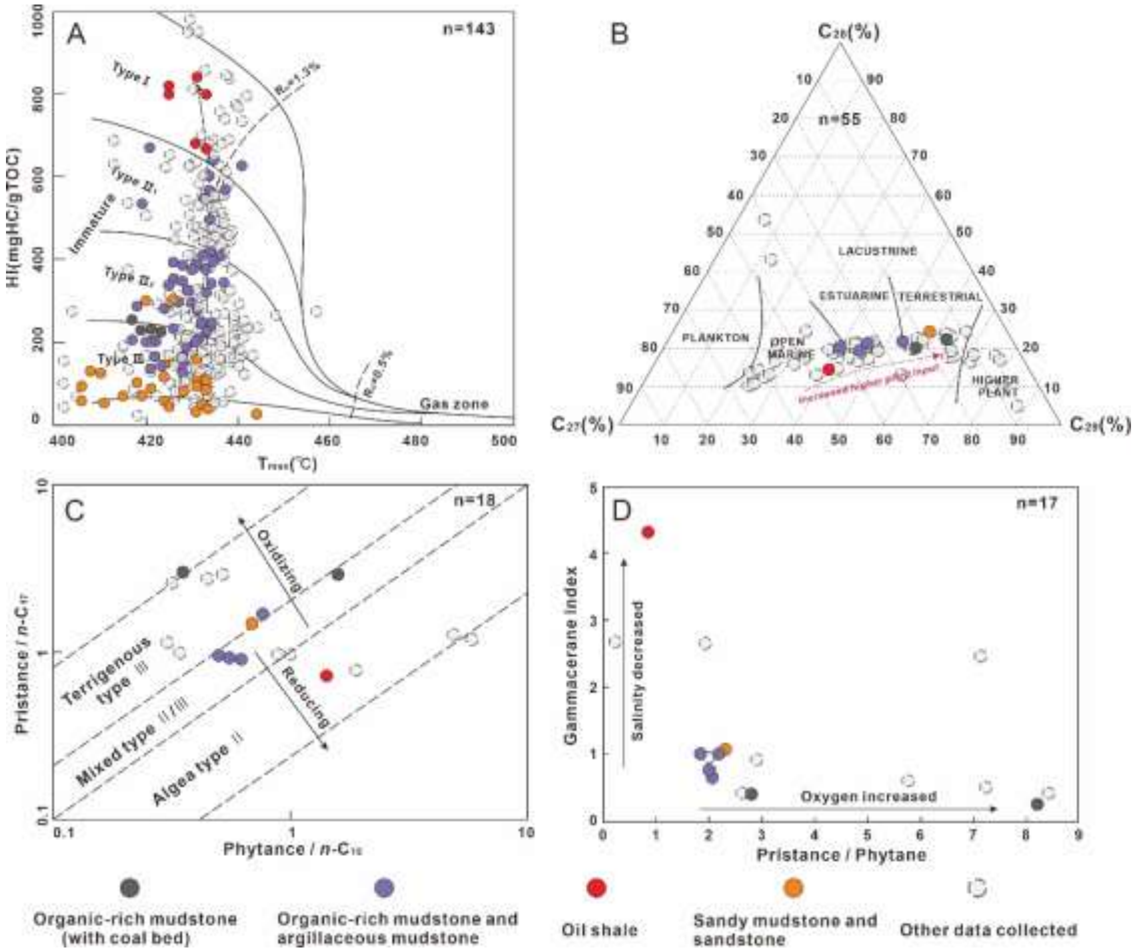

A
n=143
HI(mgHC/gTOC)
Type I
Type II1
Type II2
Type III
Immature
Ro=1.3%
Ro=0.5%
Gas zone
Tmax(℃)
B
C28(%)
C27(%)
C29(%)
n=55
LACUSTRINE
ESTUARINE
TERRESTRIAL
PLANKTON
OPEN MARINE
HIGHER PLANT
C
n=18
Pristance / n-C17
Phytance / n-C18
Oxidizing
Reducing
Terrigenous type III
Mixed type II/III
Algea type II
D
n=17
Gammacerane index
Pristance / Phytane
Salinity decreased
Oxygen increased
Organic-rich mudstone (with coal bed)
Organic-rich mudstone and argillaceous mudstone
Oil shale
Sandy mudstone and sandstone
Other data collected

Figure 9

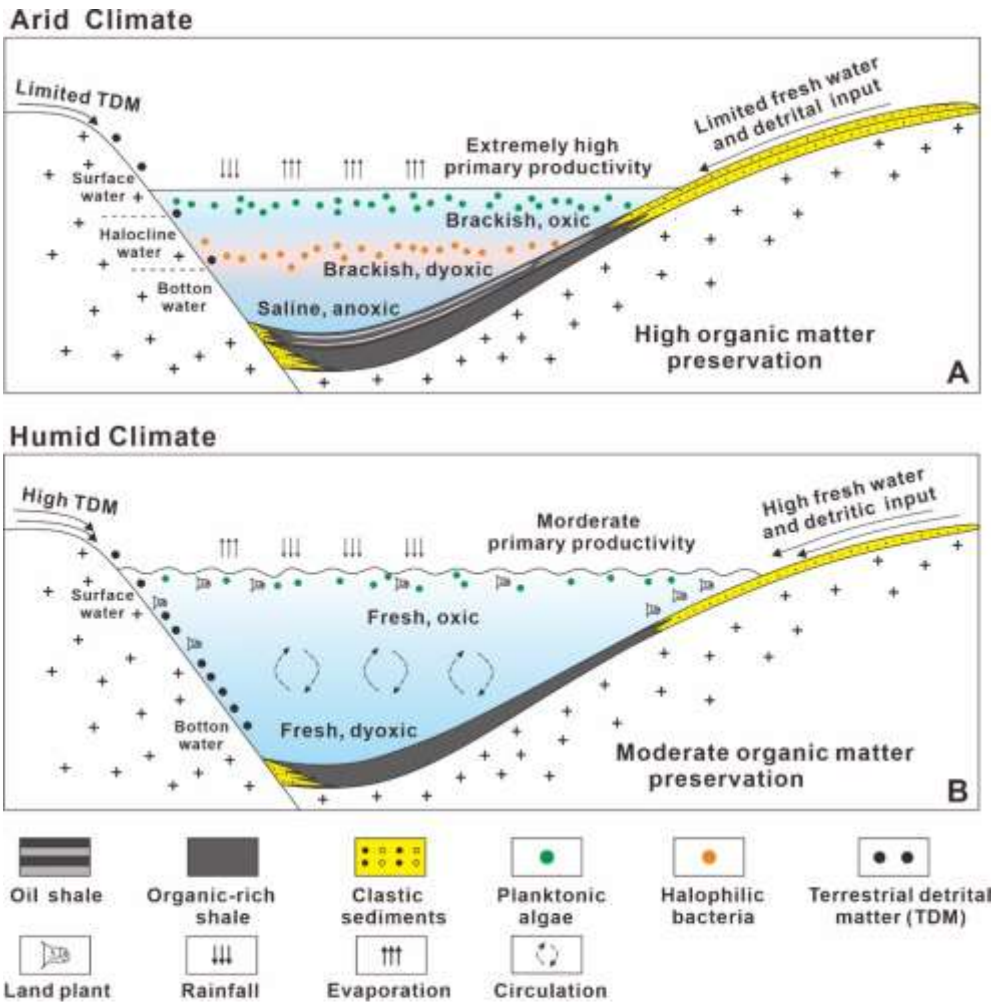

Arid Climate
Limited TDM
Limited fresh water and detrital input
Extremely high primary productivity
Surface water
Halocline water
Botton water
Brackish, oxic
Brackish, dyoxic
Saline, anoxic
High organic matter preservation
A
Humid Climate
High TDM
High fresh water and detritic input
Morderate primary productivity
Surface water
Botton water
Fresh, oxic
Fresh, dyoxic
Moderate organic matter preservation
B
Oil shale
Organic-rich shale
Clastic sediments
Planktonic algae
Halophilic bacteria
Terrestrial detrital matter (TDM)
Land plant
Rainfall
Evaporation
Circulation

Table 1

| Lithofacies | Quantities | TOC (wt%) | Average mineral content (wt%) | | | | | | | Rigid particle (wt%) | Carbonate (wt%) | Clay (wt%) |
|---|---|---|---|---|---|---|---|---|---|---|---|---|
| | | | Quartz | K-feldspar | plagioclase | Calcite | Dolomite | aragonite | siderite | | | |
| oil shale | 6 | 4.3 | 19.8 | 2.1 | 4.7 | 12.6 | 3.1 | 17.8 | 1.6 | 26.5 | 35.0 | 38.5 |
| organic-rich mudstone | 53 | 3.6 | 26.4 | 1.6 | 2.5 | 0.3 | 0 | 0 | 7.8 | 30.6 | 8.1 | 61.3 |
| argillaceous mudstone | 13 | 1.6 | 11.3 | 1.7 | 2.1 | 3.0 | 0 | 0 | 6.2 | 31.3 | 9.2 | 59.5 |
| sandy mudstone | 20 | 0.8 | 32.7 | 2.3 | 1.2 | 1.1 | 0 | 0 | 4.9 | 36.2 | 6.0 | 57.8 |

Table 2.

| Geochemical Proxies | | Oil shale | Organic-rich Mudstone | Argillaceous Mudstone | Sandy Mudstone |
|---|---|---|---|---|---|
| Quantities | | 11 | 52 | 6 | 14 |
| Fe/Mn | Min-max | 12.5-173.4 | 11.7-154.4 | 84.9-212.4 | 35.5-282.9 |
| | Average | 69.8 | 52.2 | 119.7 | 125.2 |
| Mg/Ca | Min-max | 0.1-4.1 | 1.7-7.2 | 0.9-2.6 | 0.3-5.7 |
| | Average | 1.0 | 4.3 | 1.6 | 2.8 |
| $Al_2O_3$(wt. %) | Min-max | 4.0-19.8 | 13.0-26.3 | 20.5-26.2 | 5.1-27.5 |
| | Average | 12.3 | 21.4 | 23.1 | 16.0 |
| $Ti_2O$(wt. %) | Min-max | 0.2-0.8 | 0.2-1.9 | 0.9-1.1 | 0.1-1.1 |
| | Average | 0.5 | 0.7 | 0.9 | 0.6 |
| CIA | Min-max | 66.1-81.6 | 78.7-89.0 | 82.9-88.7 | 68.1-89.9 |
| | Average | 73.9 | 85.4 | 85.6 | 82.0 |
| Sr/Ba | Min-max | 0.2-2.3 | 0.1-0.4 | 0.2-0.4 | 0.2-0.2 |
| | Average | 1.1 | 0.2 | 0.3 | 0.2 |
| Ga (ppm) | Min-max | 4.3-26.1 | 18.0-33.8 | 14.1-34.2 | 27.6-36.3 |
| | Average | 13.8 | 27.8 | 27.5 | 30.4 |
| Th/U | Min-max | 1.0-4.5 | 2.7-6.4 | 2.4-8.9 | 3.7-5.7 |
| | Average | 2.5 | 4.2 | 5.2 | 4.9 |
| V/Cr | Min-max | 1.2-1.9 | 1.1-2.0 | 0.8-2.5 | 1.2-1.5 |
| | Average | 1.5 | 1.4 | 1.37 | 1.31 |
| $Ba_{xs}$ (ppm) | Min-max | 0-523.3 | 0-301.2 | 0 | 0 |
| | Average | 197.8 | 8.1 | 0 | 0 |
| $P_{xs}$ (ppm*100) | Min-max | 0-30.2 | 0-94.1 | 0 | 0 |
| | Average | 13.9 | 6.0 | 0 | 0 |